JGR Space Physics

RESEARCH ARTICLE
10.1029/2020JA028112

MESSENGER Observations of Flow Braking and Flux Pileup of Dipolarizations in Mercury's Magnetotail: Evidence for Current Wedge Formation

Ryan M. Dewey[1], James A. Slavin[1], Jim M. Raines[1], Abigail R. Azari[1], and Weijie Sun[1]

[1]Department of Climate and Space Sciences and Engineering, University of Michigan, Ann Arbor, MI, USA

Key Points:
- Dipolarizations in Mercury's magnetotail encounter strong magnetic pressure gradients near the planet that brake their fast sunward flow
- Only a small fraction of dipolarizations reach the nightside surface; most brake and contribute to magnetic flux pileup
- Pileup results from the interaction of multiple dipolarizations and is consistent with Earth-like substorm current wedge formation

Correspondence to:
R. M. Dewey,
rmdewey@umich.edu

Citation:
Dewey, R. M., Slavin, J. A., Raines, J. M., Azari, A. R., & Sun, W. (2020). MESSENGER observations of flow braking and flux pileup of dipolarizations in Mercury's magnetotail: Evidence for current wedge formation. *Journal of Geophysical Research: Space Physics*, *125*, e2020JA028112. https://doi.org/10.1029/2020JA028112

Received 15 APR 2020
Accepted 21 AUG 2020
Accepted article online 29 AUG 2020

Abstract Similar to Earth, Mercury's magnetotail experiences frequent dipolarization of the magnetic field. These rapid (~2 s) increases in the northward component of the tail field (ΔB_z ~ 30 nT) at Mercury are associated with fast sunward flows (~200 km/s) that enhance local magnetic field convection. Differences between the two magnetospheres, namely Mercury's smaller spatiotemporal scales and lack of an ionosphere, influence the dynamics of dipolarizations in these magnetotails. At Earth, the braking of fast dipolarization flows near the inner magnetosphere accumulates magnetic flux and develops the substorm current wedge. At Mercury, flow braking and flux pileup remain open topics. In this work, we develop an automated algorithm to identify dipolarizations, which allows for statistical examination of flow braking and flux pileup in Mercury's magnetotail. We find that near the inner edge of the plasma sheet, steep magnetic pressure gradients cause substantial braking of fast dipolarization flows. The dipolarization frequency and sunward flow speed decrease significantly within a region ~500 km thick located at ~900 km altitude above Mercury's local midnight surface. Due to the close proximity of the braking region to the planet, we estimate that ~10–20% of dipolarizations may reach the nightside surface of the planet. The remaining dipolarizations exhibit prolonged statistical flux pileup within the braking region similar to large-scale dipolarization of Earth's inner magnetosphere. The existence of flow braking and flux pileup at Mercury indicates that a current wedge may form, although the limitations imposed by Mercury's magnetosphere require the braking of multiple, continuous dipolarizations for current wedge formation.

1. Introduction

Dipolarizations are common to the magnetotails of both Earth and Mercury. A product of intense nightside reconnection, dipolarizations represent newly closed, more dipolar field lines that are carried planetward by fast reconnection outflows (e.g., Fu et al., 2013; Runov et al., 2012; Sitnov et al., 2009). Observed in situ, dipolarizations are identified by the sharp, step-like increase in the northward component of the magnetic field (known as the dipolarization front, e.g., Nakamura et al., 2002) that precedes the newly reconnected flux tube (known as the dipolarizing flux bundle, Liu et al., 2013). Since dipolarizations are a result of reconnection between the low-density magnetotail lobes, they tend to be depleted in thermal plasma and embedded within fast sunward flows (e.g., Angelopoulos et al., 1992; Runov et al., 2015; Sergeev et al., 1996). Additional signatures of dipolarizations include an enhanced cross-tail electric field, enhanced thermal plasma temperature, and enhanced energetic particle flux compared to the surrounding plasma sheet (e.g., Runov et al., 2009, 2013).

At Earth, dipolarizations contribute major roles in mass and magnetic flux transport, particle acceleration, and substorm current wedge formation. Although individual dipolarizations are localized in their cross-tail extent (~1–3 R_E, where R_E is Earth's mean radius, 6,371 km), their faster sunward flow, stronger northward magnetic field, and enhanced cross-tail electric field compared to the surrounding plasma sheet result in dipolarizations transporting the majority of magnetic flux from the midtail to the near-tail, particularly during geomagnetically active intervals (Liu et al., 2014). As a dipolarization travels planetward, particles interacting with its magnetic structure, particularly those trapped by the local magnetic field gradients about the dipolarization front, can experience betatron and Fermi acceleration (e.g., Ashour-Abdalla et al., 2011; Birn et al., 2013; Gabrielse et al., 2016; Ukhorskiy et al., 2018). Only a small fraction of dipolarizations penetrate into the inner magnetosphere, with the majority of dipolarizations stopping near the inner edge of the

plasma sheet (Dubyagin et al., 2011; Ohtani et al., 2006; Shiokawa et al., 1997). Near this boundary, dipolarizations brake due to steep magnetic pressure gradients, and their magnetic flux accumulates (or piles up) (Birn et al., 2011; Karlsson et al., 2015). As additional dipolarizations brake and accumulate, this flux pileup region can expand both azimuthally and downtail, resulting in a large-scale dipolarization of the near-tail region (e.g., Baumjohann et al., 1999; Birn et al., 2011, 2019; Merkin et al., 2019). The flux pileup structure is supported by the substorm current wedge, which diverts the cross-tail current into the ionosphere via field-aligned currents of the Region 1-sense (e.g., Birn et al., 1999; Kepko, Glassmeier, et al., 2015; McPherron et al., 1973). The exact mechanics by which dipolarizations (both small- and large-scale) establish and maintain the substorm current wedge have been the subject of considerable interest and debate. A contemporary understanding is the "wedgelet" conceptual model in which the individual field-aligned current systems of many small-scale dipolarizations manifest into the substorm current wedge as the dipolarizations brake near the inner magnetosphere (e.g., Birn et al., 2019; Liu et al., 2013; Sun et al., 2013). In this understanding, the current wedge is not a single, monolithic current loop, but that its trending structure emerges from the complex interaction between individual dipolarization current systems.

Mercury possesses a terrestrial-like magnetosphere, but it operates at substantially smaller spatiotemporal scales, experiences stronger effects from magnetic reconnection, and couples to a different type of inner magnetospheric boundary than Earth's magnetosphere. Mercury's magnetosphere contains many of the same regions as Earth's, including a closed dayside region and an extended magnetotail (see Korth et al., 2018 and Slavin et al., 2018 for comprehensive reviews). Mercury's planetary magnetic field, however, is only ~1% the strength of Earth's (e.g., Anderson et al., 2011), which when combined with the stronger upstream solar wind dynamic pressure at Mercury's orbital location results in a magnetosphere substantially smaller in both absolute and relative scales. For example, Mercury's subsolar magnetopause stands at ~0.5 $R_M \approx$ 1,200 km altitude above the planet's dayside surface (Winslow et al., 2013), where R_M is Mercury's mean radius (2,440 km). By contrast, Earth's subsolar magnetopause stands at ~10 $R_E \approx$ 64,000 km altitude (e.g., Shue et al., 1998). Furthermore, the cross-tail extent of Mercury's magnetotail is ~4 $R_M \approx$ 10,000 km compared to Earth's of ~40 $R_E \approx$ 255,000 km (Kaymaz et al., 1992; Rong et al., 2018; Slavin et al., 2012). Consequences of the small dimensions of Mercury's magnetosphere include increased finite gyroradius effects (particularly for heavy ions of planetary origin), increased loss due to surface precipitation, and an increased fraction of the magnetosphere occupied by the planet (e.g., Delcourt, 2013; Delcourt et al., 2003; Ogilvie et al., 1977; Raines et al., 2014). Mercury's hypothetical plasmapause, for example, would be located below the planet's surface due to the planet occupying a large fraction of the magnetosphere and the planet's slow ~59-day rotation. Mercury's magnetosphere also experiences stronger effects from magnetic reconnection. The lower solar wind Alfvén Mach number at Mercury's orbital location results in the formation of thick plasma depletion layers within Mercury's magnetosheath adjacent to the magnetopause (Gershman et al., 2013). These depletion layers allow for more frequent and stronger subsolar magnetopause reconnection that is less sensitive to the direction of the interplanetary magnetic field than at Earth (DiBraccio et al., 2013). Dayside reconnection powers Mercury's ~3 min Dungey cycle and many of the observed dynamics within the magnetosphere (e.g., Imber & Slavin, 2017; Slavin et al., 2009, 2010, 2018). Finally, Mercury's large conducting core plays a unique role in magnetospheric dynamics by acting as the magnetosphere's innermost boundary. Mercury lacks an ionosphere so it is expected that its large core (~2,000 km in radius) provides current-closure for static and/or large-scale field-aligned current systems (e.g., Anderson et al., 2014; Janhunen & Kallio, 2004). These current systems pass radially through the thin (~400 km) layer of resistive regolith to connect over the surface of the conducting core. Mercury's core also influences the magnetosphere's interaction with the solar wind. Changes in the solar wind dynamic pressure induce currents on the core's surface that modify the planet's magnetic moment to resist these changes (e.g., Jia et al., 2015, 2019; Johnson et al., 2016; Slavin et al., 2014). Although similar responsive currents may also be induced on the surface of Earth's core, these currents are substantially stronger at Mercury due to Mercury's relatively larger core and the core's close proximity to the magnetopause.

Given the similar topology between Mercury and Earth's magnetospheres and the dominance of magnetic reconnection in Mercury's dynamics, it is not surprising that dipolarizations are common in Mercury's magnetotail. Similar to those identified at Earth, dipolarizations at Mercury are characterized by a rapid (~2 s) increase in the northward component of the magnetic field (~30 nT) that persists for a short time (~10 s) (Sundberg et al., 2012). Observations from the MESSENGER spacecraft have associated dipolarizations in

Mercury's magnetotail with thermal plasma depletion and heating, fast sunward flows, and energetic electron acceleration and injection (Dewey, Slavin, et al., 2017, 2018; Sun et al., 2018). While Mercury's dipolarizations share many similar features to those at Earth, they also display curious differences. Dipolarizations, for example, are more frequent to Mercury's postmidnight magnetotail, opposite to that of Earth (Sun et al., 2016). Studies of dipolarizations at Mercury have made considerable progress in understanding the signatures and characteristics of these events, yet the dynamics and consequences of Mercury's dipolarizations remain less well understood. One such topic is that of flow braking. Mercury's near-planet reconnection site, located at or planetward of $X_{\mathrm{MSM}'} = -3\ R_{\mathrm{M}}$, is only ~5,000 km above the planet's nightside surface (e.g., DiBraccio et al., 2015; Poh et al., 2017a; Slavin et al., 2009; Smith et al., 2017). Even smaller yet is the distance between the inner edge of Mercury's current sheet and the planet's surface (~500–750 km) (Poh et al., 2017a). Over these distances, the magnetic field increases by a factor of only ~10–100 due to Mercury's weak planetary magnetic field and the large volume of the magnetosphere that the planet occupies. By contrast, the magnetic field at Earth's surface is ~10,000 times greater than in the magnetotail. Is Mercury's magnetic field strong enough to brake dipolarizations and their fast flows? Or do dipolarizations stream directly into the planet's nightside surface unencumbered by the relatively weak magnetic gradients? The answers to these questions carry significance for mass and magnetic flux transport, but are also interdisciplinary, with consequences for exospheric generation and space weathering.

Initial investigations suggest that braking is likely to occur although the mechanism and location of braking are poorly constrained. Sun et al. (2015) provided the first evidence for flow braking in Mercury's magnetotail by analyzing case studies of Alfvén and compressional waves associated with dipolarizations near the planet, interpreting them to be similar to the waves generated by the braking of flows in Earth's magnetotail (e.g., Panov et al., 2014). At that time, however, the association of Mercury's dipolarizations with fast sunward flows was only speculated. Dewey et al. (2018) established the connection between fast flows and dipolarizations at Mercury by developing a technique to determine average flows by combining together plasma observations of many individual dipolarizations. On the basis of pressure balance, Dewey et al. (2018) hypothesized that these fast flows would break at or planetward of $X_{\mathrm{MSM}'} = -1.3\ R_{\mathrm{M}}$, near the expected inner edge of the current sheet (e.g., Poh et al., 2017a). Due to the limited sample size of dipolarizations, however, Dewey et al. (2018) was unable to examine the behavior of flows as a function of location in Mercury's magnetotail and could not support their hypothesis of braking directly. Finally, Poh et al. (2017b) investigated a signature suggestive of magnetic flux pileup within Mercury's midnight current sheet. Poh et al. (2017b) selected current sheet crossings on their ability to be fit by a one-dimensional Harris current sheet and noticed an enhancement of B_z local to midnight between $-1.4 < X_{\mathrm{MSM}'} < -1.7\ R_{\mathrm{M}}$. The authors interpreted the B_z enhancement as being due to a current wedge similar to Earth's; however, their work does not connect such a signature to dipolarizations, fast flows, or substorm dynamics. These studies have provided valuable foundational observations and discussions into the topics of flow braking and flux pileup in Mercury's magnetotail but leave the topic largely unconstrained.

In this study, we expand upon previous observations and discussions of flow braking and flux pileup in Mercury's magnetotail. We develop an automated algorithm to identify dipolarizations in the magnetic field time series to expand the sample size of events to over an order of magnitude previously examined. This large sample size allows us to employ statistical techniques and form a statistical description of flow braking in lieu of multipoint spacecraft observations. We find that the majority (~80–90%) of dipolarizations brake within a thin (~500 km) region located close to Mercury's surface (~900 km altitude) due to magnetic pressure gradients from the planet's dipole magnetic field. As these flows brake, we observe statistically that their magnetic flux accumulates to form a pileup region that may be associated with an Earth-like current wedge. In section 2, we describe our data sources and briefly introduce the dipolarization identification algorithm (described in detail in Appendix A). In section 3, we present both statistical and case study analysis of flow braking and flux pileup, followed by a discussion of these results and the possibility of current wedge formation at Mercury in section 4. We conclude this investigation in section 5 with avenues for further research.

2. Methodology and Data Sources

For this investigation, we rely on observations from MESSENGER's Magnetometer (MAG; Anderson et al., 2007) and Fast Imaging Plasma Spectrometer (FIPS; Andrews et al., 2007). The MAG instrument

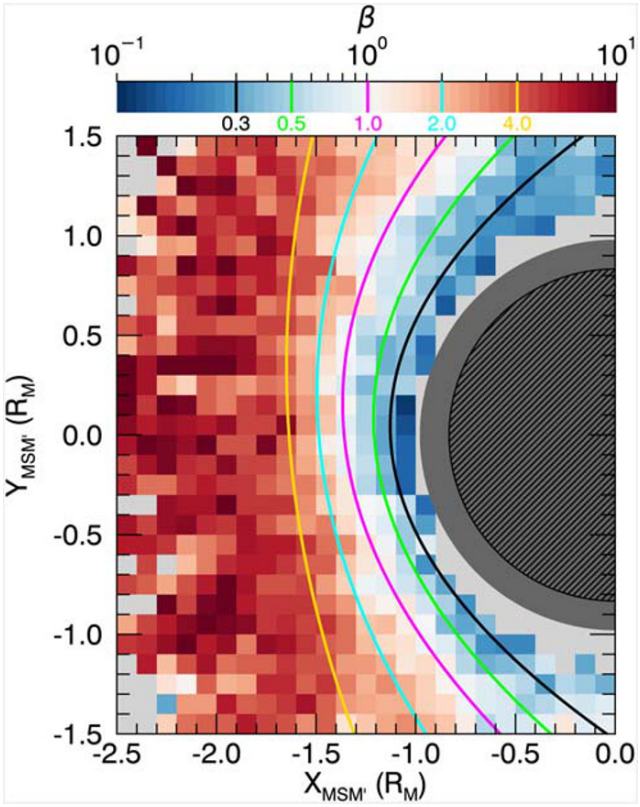

Figure 1. Equatorial distribution of proton plasma beta (β) as indicated by the color bar. Light gray bins indicate regions of insufficient sampling (<6 FIPS scans, corresponding to <2 min of sampling). The dark gray indicates Mercury's nightside surface and the black-hatched region denotes its conducting core. The five color polynomials (black, lime, magenta, cyan, and gold) are contours of specific β (0.3, 0.5, 1.0, 2.0, and 4.0), as indicated by the vertical lines of the corresponding color in the color bar.

measures the local vector magnetic field at 50 ms time resolution. The FIPS sensor measures thermal and low-energy ions with energy-per-charge (e/q) spanning 50 eV/e to 13 keV/e and mass-per-charge (m/q) spanning 1 to 40 amu/e. FIPS completes a nominal sweep of its energy steps in 10 s. While FIPS has a large instantaneous field of view (~1.1π sr), it is unable to measure bulk plasma flows at its native resolution since the spacecraft is three-axis stabilized. To estimate flows, we rely on a statistical reconstruction technique developed by Dewey et al. (2018). This technique assumes that plasma flows are subsonic and utilizes variable field of view pointing across many FIPS scans to construct a more complete velocity space distribution from which bulk plasma flows and their uncertainty can be determined. We refer readers to Dewey et al. (2018) for a technical description and example of this procedure. In Appendix B, we provide a summary of the flow-determination procedure and discuss its application to partial velocity space distributions. We display all MESSENGER observations in the aberrated Mercury solar magnetospheric (MSM′) coordinate system, which is centered at Mercury's dipole center with $X_{MSM'}$ pointing antiparallel to the solar wind (a radial solar wind speed of 400 km/s is assumed), $Z_{MSM'}$ pointing northward, and $Y_{MSM'}$ completing the right-handed system.

To identify dipolarizations, we rely exclusively on the MAG observations. While several dipolarization signatures are related to the thermal plasma, a complete FIPS scan has time resolution comparable to the typical duration of a dipolarization (Dewey, Slavin, et al., 2017) and therefore cannot resolve these signatures for all dipolarizations. MAG observations, in contrast, are able to resolve the magnetic field structure of the dipolarization at native resolution. Of the magnetic field signatures of a dipolarization, the sharp, step-like increase in B_z of the dipolarization front is the easiest to detect (e.g., Liu et al., 2013; Sun et al., 2016). We develop an automated algorithm to identify dipolarization fronts in the B_z time series. The algorithm, described in detail in Appendix A, evaluates each point in the time series for a strong, positive, coherent, local gradient in B_z and applies a series of physical tests to determine if such a slope is representative of a dipolarization front or not.

We apply our dipolarization selection procedure to 1,946 magnetotail intervals that satisfy several criteria. First, to ensure that we are examining the plasma sheet rather than the adjacent magnetotail lobes, we require the 1-min running average $B_z/|B| > 0.5$ and $\beta > 0.1$, where β is the proton plasma beta. These criteria estimate that the spacecraft samples the closed, mass-loaded magnetic field lines characteristic of the plasma sheet. Other studies of Mercury's magnetotail have used β to identify plasma sheet intervals (e.g., Poh et al., 2018; Sun et al., 2017), but they typically use a higher β threshold. We use a lower threshold since FIPS may underestimate the local plasma beta in the presence of the fast flows associated with dipolarizations (e.g., Dewey et al., 2018) due to the sensor's limited field of view. Second, we exclude intervals contaminated by solar energetic particle events. Third, we limit our survey to the spatial region $-2.5 < X_{MSM'} < 0$,$|Y_{MSM'}| < 1.5$, and $|Z_{MSM'}| < 0.2\ R_M$. Finally, to prevent biasing from short intervals, we require that the criteria above must be met for longer than 3 min (the nominal Dungey cycle duration). Together, these 1,946 magnetotail intervals represent an accumulated 14,022 min of observation from which 5,178 dipolarizations are identified. This event sample size is an order of magnitude larger than previously examined at Mercury (e.g., Dewey et al., 2018) and allows us to employ statistical techniques to examine the characteristics of dipolarizations as a function of spatial location in Mercury's magnetotail (section 3).

To provide context to the dipolarization observations described in later sections, we determine the average proton plasma beta (β) as a function of spatial location in Mercury's magnetic equatorial plane, as shown in Figure 1. To construct this distribution, we compute the average magnetic field, proton density, and

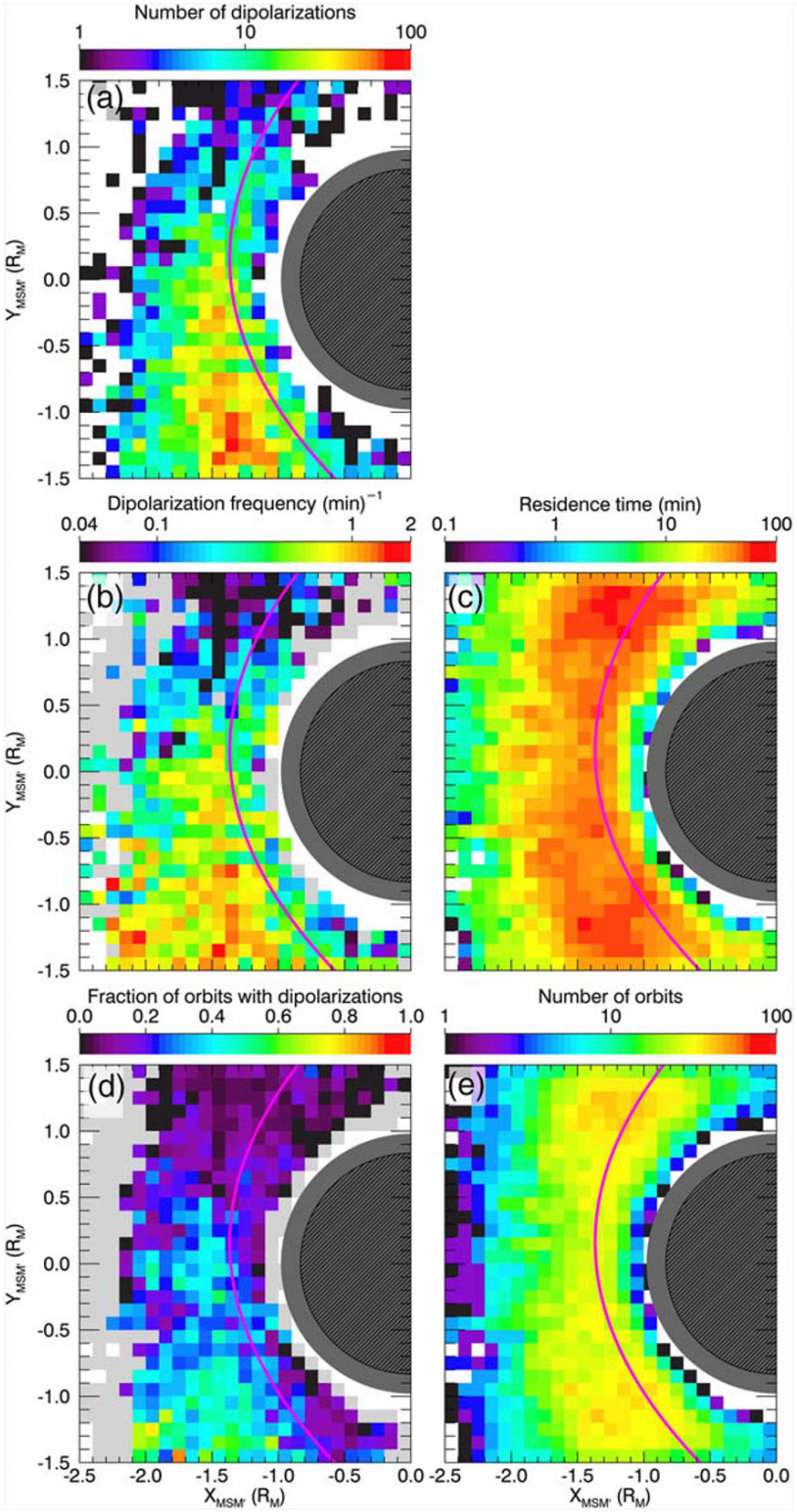

Figure 2. Equatorial distributions in the same format as Figure 1. (a) Number of dipolarizations, where white indicates no dipolarizations observed. (b) Frequency of dipolarizations, where light gray indicates no dipolarizations observed and white indicates insufficient sampling time (<1 min). (c) Spacecraft sampling time, where white indicates regions of no samples. (d) Fraction of orbits that contain dipolarizations within that spatial bin, where light gray indicates insufficient sampling (<3 orbits) and white indicates regions of no sampling. (e) Number of orbits, where white indicates regions of no samples. The magenta polynomial in each panel corresponds to the $\beta = 1$ contour from Figure 1.

proton temperature under the assumption of isotropy (e.g., Gershman et al., 2013; Raines et al., 2011) for each FIPS scan within the 1,946 intervals (84,187 scans total). We then use the spacecraft's location at the center of each scan to sort scans into a two dimensional ($X_{MSM'}$, $Y_{MSM'}$) histogram. Within each histogram bin, we determine the mean proton density, proton temperature, and magnetic field strength from the scans assigned to that bin, from which plasma beta is then calculated. We propagate uncertainties, which are typically on the order of 1–5% for magnetic field strength and 10–20% for proton density and temperature. For five specific values of β (0.3, 0.5, 1.0, 2.0, and 4.0) we determine contours within the spatial distribution and display polynomial fits to those contours (black, lime, magenta, cyan, and gold, respectively). Each contour is well represented by a second-order polynomial (χ^2 values of 0.045, 0.049, 0.029, 0.033, and 0.019, respectively). As expected for the plasma sheet, $\beta \gg 1$ far from the center of the planetary dipole with contours nearly parallel to $Y_{MSM'}$. Approaching the planet, β decreases and contours bow about the planetary magnetic field, with $\beta \ll 1$ close the dipole center. For reference, at local midnight, $\beta = 1$ (magenta line) at $X_{MSM'} \approx -1.36\ R_M$, approximately 900 km in altitude above the nightside surface. Plasma beta also displays a cross-tail asymmetry, with systematically greater values in the postmidnight plasma sheet. This asymmetry can be observed by noticing that the β contours in the postmidnight plasma sheet are located at greater $X_{MSM'}$ values than those in the premidnight plasma sheet. For example, at $Y_{MSM'} = -1\ R_M$ the $\beta = 1$ contour is located at $X_{MSM'} \approx -0.98\ R_M$ while at $Y_{MSM'} = +1\ R_M$ the same contour is located at $X_{MSM'} \approx -1.16\ R_M$. This cross-tail asymmetry is among other asymmetries noted in plasma and magnetic field parameters in Mercury's central plasma sheet (e.g., Korth et al., 2014; Poh et al., 2017b; Raines et al., 2013; Rong et al., 2018).

3. Results

3.1. Observations of Flow Braking

To determine if dipolarizations impact Mercury's nightside surface directly or if they brake/divert before then, we begin by examining the distribution of dipolarization occurrence as a function of location within Mercury's magnetotail. Figure 2a displays the number of dipolarizations identified by the automated procedure of section 2 as a function of equatorial ($X_{MSM'}$, $Y_{MSM'}$) location. As a function of $Y_{MSM'}$, dipolarizations display a strong cross-tail asymmetry with over an order of magnitude more dipolarizations observed postmidnight than premidnight similar to the findings of other studies (Dewey et al., 2018; Sun et al., 2016). The range $-1.5 < Y_{MSM'} < 0.5\ R_M$ contains 90.7% of the identified dipolarizations. As a function of $X_{MSM'}$, the number of dipolarizations drops sharply planetward of the $\beta = 1$ contour (magenta line), particularly in the postmidnight magnetotail. Few dipolarizations are observed tailward of $X_{MSM'} = -2\ R_M$.

To account for effects from nonuniform spacecraft sampling, we display the frequency of dipolarizations within Figure 2b. To produce this distribution, we divide the number of dipolarizations observed within each spatial bin (Figure 2a) by the total time the spacecraft was at that location during the 1,946 intervals (Figure 2c). Examining the frequency of dipolarizations, the strong cross-tail asymmetry persists. The apparent decrease in dipolarizations tailward of $X_{MSM'} = -2\ R_M$, however, is removed after correcting for spacecraft sampling. Dipolarizations possess an approximately uniform frequency tailward of the $\beta = 1$ contour for $Y_{MSM'} < -0.5\ R_M$. The decrease in number of dipolarizations sunward of $\beta = 1$ does not appear to be an artifact of spacecraft sampling. Where dipolarizations are most frequent ($-1.5 < Y_{MSM'} < 0.5\ R_M$), the frequency decreases by an order of magnitude about $\beta = 1$. For $Y_{MSM'} < -0.5\ R_M$, the frequency tailward of $\beta = 1$ is ~1–2 dipolarizations per minute, falling to ~0.1–0.2 closer to the planet. The trend is less clear at local midnight ($-0.5 < Y_{MSM'} < 0.5\ R_M$). The frequency tailward of $\beta = 1$ is ~1 dipolarization per minute, and while there are several bins planetward of $\beta = 1$ that reach similar frequencies, there is considerable scatter, with many bins observing dipolarizations at a rate of ~0.2 per minute and many others observing no dipolarizations at all (light gray).

As will be described in further detail below (Figure 7), when dipolarizations are observed, they tend to be observed in series with other dipolarizations. This trend has been anecdotally described in other studies involving dipolarizations at Mercury (e.g., Dewey, Slavin, et al., 2017, 2018; Sundberg et al., 2012; Sun et al., 2020). An effect of dipolarizations typically appearing in groups is that it can skew event frequency. We therefore use the fraction of orbits that contain dipolarizations (Figure 2d) as a metric complementary to event frequency. To produce this distribution, for each spatial bin, we determine the number of orbits

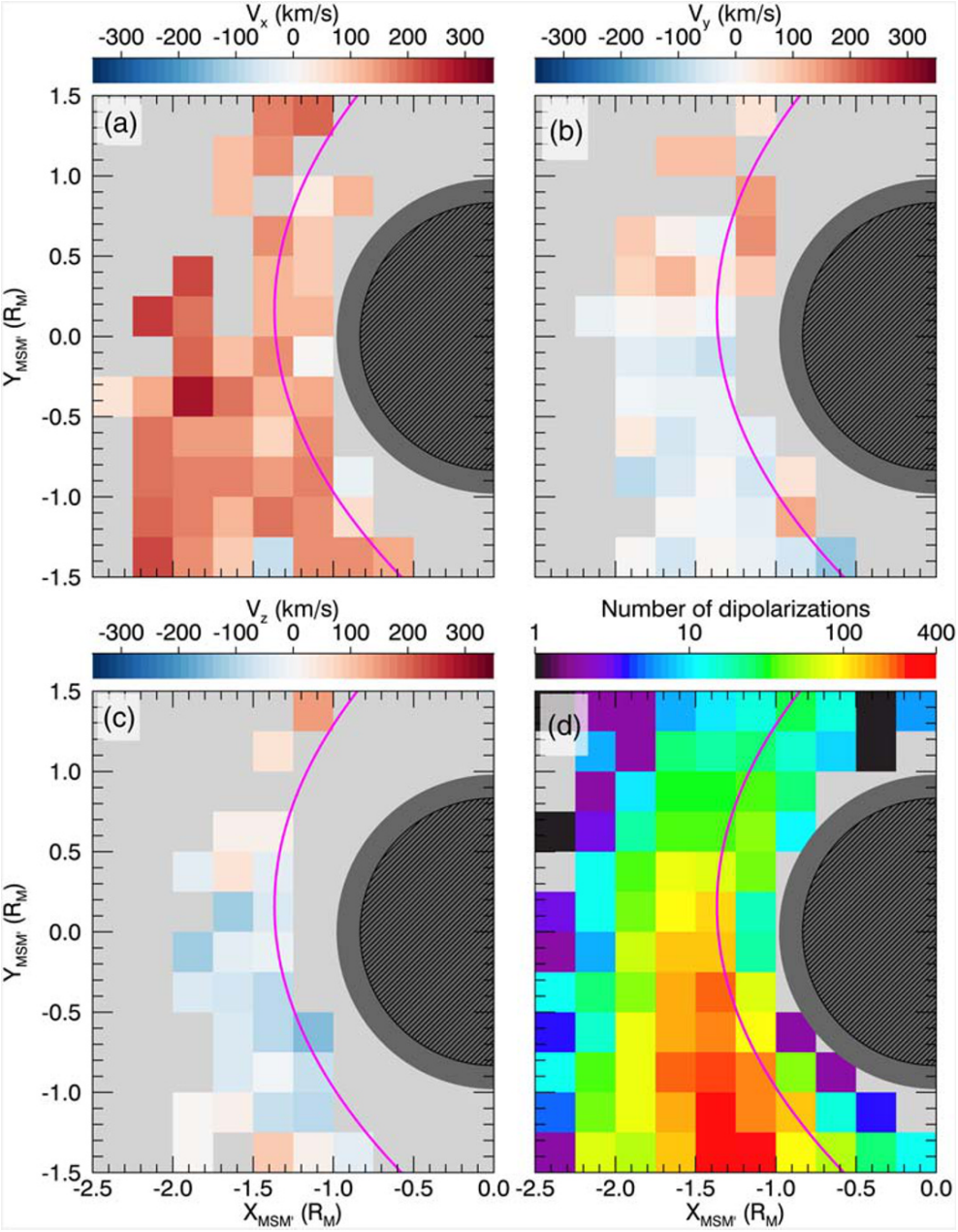

Figure 3. Typical dipolarization flow components as a function of equatorial location in the same format as Figure 2. (a) Sunward component (V_x), (b) duskward component (V_y), (c) northward component (V_z), and (d) number of dipolarizations used to determine these flows. Light gray bins in (a)–(c) indicate spatial locations whose flow component in that direction could not be determined reliably (see Appendix B). Light gray bins in (d) indicate regions with no dipolarizations.

that contain one or more dipolarizations within that bin and divide it by the total number of orbits that sampled that bin (Figure 2e). Similar to conventional frequency (Figure 2b), the cross-tail asymmetry in dipolarization occurrence persists. Postmidnight, a greater fraction of orbits (~0.4–0.7) contain dipolarizations than premidnight (~0.1). About $\beta = 1$, the fraction of orbits that contain dipolarizations also drops substantially. Where dipolarizations are most common ($-1.5 < Y_{MSM'} < 0.5\ R_M$), the fraction of orbits with dipolarizations decreases from ~0.4–0.5 just tailward of $\beta = 1$ to ~0.1 planetward of the contour. The only location within this $Y_{MSM'}$ range that does not appear to follow this trend is at $Y_{MSM'} = -0.5\ R_M$ where the fraction of orbits with dipolarizations (~0.4) remains unchanged about $\beta = 1$.

Taken together, these trends in dipolarization occurrence imply that they do not typically reach Mercury's nightside surface. If dipolarizations usually impacted the planet, we should expect the rate at which dipolarizations are observed to remain approximately constant up to the planet's surface. Rather, we observe that the rate of dipolarization occurrence (interpreted either as the frequency of dipolarizations or as the fraction of orbits that contain dipolarizations) decreases sharply about the $\beta = 1$ contour, which is located ~900 km altitude above the nightside surface. If dipolarizations do indeed divert or brake before reaching the nightside surface, these signatures should be apparent in the flows associated with dipolarizations. As described in section 2, FIPS cannot determine flows at its nominal time resolution, however, we can follow the procedure developed by Dewey et al. (2018) to examine flows statistically. We refer readers to Dewey et al. (2018) for technical details of this procedure. While Dewey et al. (2018) used 387 dipolarizations spread throughout Mercury's magnetotail to obtain a single representative flow, we can leverage our increased event sample size to determine statistical flows as a function of spatial location, enabling us to examine plasma signatures of flow breaking.

In Figure 3, we apply the Dewey et al. (2018) flow-determination technique to FIPS observations of dipolarizations. For each spatial bin, we first identify all dipolarizations that were observed within that area of the magnetotail, then we select all FIPS scans that cover the end of each of those event's dipolarization fronts, and finally, we apply the Dewey et al. (2018) technique to those scans to determine average flows. Figure 3a displays the sunward component of these flows (V_x), Figure 3b the duskward component (V_y), Figure 3c the northward component (V_z), and Figure 3d the number of dipolarizations. In calculating these statistical flows, we evaluate uncertainty from statistical and systematic sources as well as uncertainty resulting from unobserved regions of velocity space (see Appendix B and Dewey et al., 2018). While some spatial bins in Figure 3d have up to 400 dipolarizations, many have between 50 and 100. The number of dipolarizations used to determine statistical flows is smaller on average than that used by Dewey et al. (2018), which results in larger uncertainties as well as prevents some flow components from being reliably determined (gray bins in Figures 3a–3c). In Appendix B, we describe quantitatively the conditions under which we do not display flow components. Including each of the sources of uncertainty described above, typical absolute and relative uncertainties for each velocity component shown in Figure 3 are 32 ± 9 km/s or (25 ± 7)% in V_x, 22 ± 10 km/s or (47 ± 22)% in V_y, and 15 ± 8 km/s or (35 ± 19)% in V_z. Finally, we expect proton flows to be representative of dipolarization transport. Dipolarizations have dimensions ~2,000 km in $X_{\mathrm{MSM'}}$ and ~750 km in $Y_{\mathrm{MSM'}}$ (see section 3.3), which are greater than the typical proton gyroradius about dipolarizations (~300 km for a 4 keV proton in a 30 nT magnetic field), indicating that the frozen-in condition is valid.

The flows in Figure 3 are indicative of both flow braking and diversion. Tailward of $\beta = 1$, V_x is dominant with speeds around 200 km/s in the sunward direction, similar to the dipolarization flow determined by Dewey et al. (2018). V_y shows a general separation about midnight tailward of $\beta = 1$ although there is considerable scatter. The mean, median, and standard deviation of V_y flows premidnight is 89, 59, and 97 km/s, respectively, compared to −59, −54, and 66 km/s postmidnight. A linear fit of V_y versus $Y_{\mathrm{MSM'}}$ yields a slope of 38 ± 4 km/s $R_{\mathrm{M}}{}^{-1}$ with a correlation coefficient of 0.62. The large variance among V_y flows suggests that V_y can vary substantially between individual dipolarizations but with a general trend of $+V_y$ flows premidnight and $-V_y$ flows postmidnight. Flows along $Z_{\mathrm{MSM'}}$ are generally negative about local midnight and positive closer to the flanks of the magnetotail, and are of the same approximate strength as V_y. Planetward of $\beta = 1$, the sunward component decreases in magnitude. This trend is most apparent for $-1 < Y_{\mathrm{MSM'}} < 0\ R_{\mathrm{M}}$, where V_x decreases from ~100–200 km/s to ~0–50 km/s about $\beta = 1$. While V_z cannot be reliably determined planetward of $\beta = 1$, V_y appears to become systematically duskward with an average value of 53 ± 31 km/s. These V_x and V_y flow signatures are indicative of both flow braking and diversion.

Figure 4 displays trends along $X_{\mathrm{MSM'}}$ more clearly. Each panel examines plasma or magnetic field parameter(s) averaged over $-1.5 < Y_{\mathrm{MSM'}} < 0.5\ R_{\mathrm{M}}$ (where dipolarizations are most common) as a function of $\Delta X_{\mathrm{MSM'}}$. $\Delta X_{\mathrm{MSM'}}$ is the distance along $X_{\mathrm{MSM'}}$ from the $\beta = 1$ contour (i.e., $\Delta X_{\mathrm{MSM'}} = 0$ lies on the $\beta = 1$ contour, with $\Delta X_{\mathrm{MSM'}} > 0$ planetward of the contour). Figure 4a examines the frequency of dipolarizations organized by $\Delta X_{\mathrm{MSM'}}$. Similar to the observations discussed with Figure 2, the frequency of dipolarizations remains approximately constant until $\beta = 1$. For $-1.5 < \Delta X_{\mathrm{MSM'}} < 0\ R_{\mathrm{M}}$, the dipolarization frequency fluctuates but remains about 0.6 min^{-1} (shaded gray region) until decreasing significantly at $\Delta X_{\mathrm{MSM'}} \approx 0$. By the $\beta = 0.5$ contour (lime), the frequency has dropped to half its downtail value. Further planetward, the

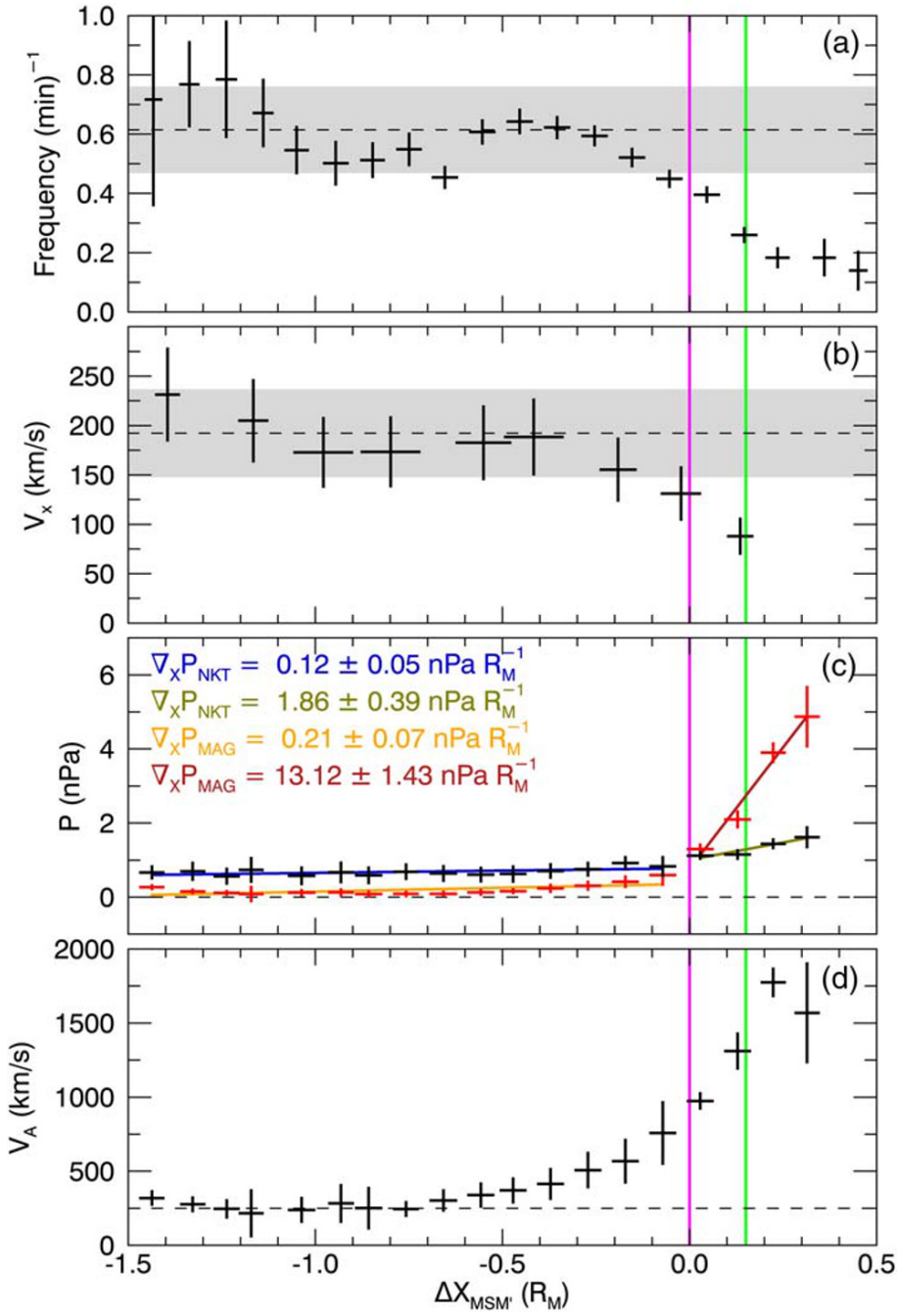

Figure 4. (a) Dipolarization frequency, (b) typical dipolarization sunward flow, (c) magnetic (P_{MAG}) and thermal proton (P_{NKT}) pressures, and (d) Alfvén speed as functions of $\Delta X_{MSM'}$ (defined in the text). The vertical magenta line corresponds to the location of the $\beta = 1$ contour and the vertical lime line corresponds to the location of the $\beta = 0.5$ contour (see Figure 1). In (a) and (b), the horizontal dashed lines and gray boxes correspond to the average and uncertainty of dipolarization frequency and sunward flow speed for $-1.5 < \Delta X_{MSM'} < 0\ R_M$. In (c), the horizontal dashed line corresponds to a pressure of zero, while the colored lines correspond to linear fits whose slopes are listed. In (d), the horizontal dashed line corresponds to a speed of 250 km/s.

frequency continues to drop to ~0.1 min^{-1}, suggesting that only a small fraction (~10–20%) of dipolarizations may impact the nightside surface directly. The sunward flow component V_x in Figure 4b displays a similar trend. For $-1.5 < \Delta X_{MSM'} < 0\ R_M$, the sunward flow speed fluctuates but remains about 192 km/s (horizontal dashed line) before beginning to decrease meaningfully at $\Delta X_{MSM'} \approx 0$. By

the $\beta = 0.5$ contour, the sunward flow has decreased to approximately half its downtail value. The dipolarization frequency and flow speed decreasing to half their respective downtail values by $\Delta X_{MSM'} \approx 0.15\ R_M$ suggests the braking region has a downtail extent of ~500 km and begins at $\beta = 1$ (an altitude of ~900 km at local midnight).

To understand the mechanism causing braking to occur in Mercury's magnetotail, Figure 4c examines proton plasma pressure and magnetic pressure as functions of $\Delta X_{MSM'}$. We follow the same general procedure in determining these pressures as for the proton plasma beta within section 2. In order to examine conditions that dipolarizations encounter, we use only FIPS and MAG measurements belonging to orbits that contain one or more dipolarization. For $\Delta X_{MSM'} < 0$, both plasma and magnetic pressures remain small (<1 nPa) with the plasma pressure dominating magnetic pressure (consistent with $\beta > 1$). At $\Delta X_{MSM'} = 0$, both pressures are within uncertainty of each other ($\beta = 1$). For $\Delta X_{MSM'} > 0$, magnetic pressure dominates plasma pressure ($\beta < 1$) as we move closer to Mercury's dipole center. Using these one-dimensional pressure profiles, we can estimate the pressure gradient forces in the sunward direction. For both $\Delta X_{MSM'} < 0$ and $\Delta X_{MSM'} > 0$, we apply linear fits to both the magnetic and plasma pressure profiles with the slope of the fit indicating the force density. For $\Delta X_{MSM'} < 0$, both magnetic and plasma pressure gradients are small (~0.1–0.2 nPa R_M^{-1}) and are within uncertainty of each other. At $\Delta X_{MSM'} = 0$, the magnetic pressure gradient increases by a factor of 60 ± 20 and the plasma pressure gradient increases by a more modest factor of 16 ± 7. The strong pressure gradients, particularly in magnetic pressure, coincident with the decreases in dipolarization occurrence and flow speed suggest dipolarizations and their associated fast flows brake as a result of the strong magnetic pressure gradients of Mercury's dipole magnetic field. Finally, Figure 4d displays the local Alfvén speed (V_A) as a function of $\Delta X_{MSM'}$. We do not incorporate heavy planetary ion species (e.g., Na+) in calculating the V_A and find that including them would not reduce V_A significantly. We will use V_A in the discussion of current wedge formation in section 4. For now, we illustrate that dipolarizations far downtail of the braking region ($\Delta X_{MSM'} < -1\ R_M$) typically travel near the local Alfvén speed, consistent with magnetic structures created from magnetic reconnection.

3.2. Observations of Flux Pileup

Observations of dipolarization frequency and flow speed in section 3.1 establish that dipolarizations typically brake before reaching Mercury's nightside surface. Within this section, we investigate whether the flow braking of dipolarizations is associated with magnetic flux pileup. We begin by first examining dipolarization profiles as a function of location within Mercury's magnetotail, similar to the frequency maps of Figure 2 and the flow maps of Figure 3. In Figure 5, we examine the northward component of the magnetic field (B_z) following dipolarizations. We standardize dipolarizations by converting to new time and magnetic field coordinates. For time, we use t, which is the time in seconds local to the midpoint of a dipolarization front (i.e., the midpoint of a dipolarization front is defined to be $t = 0$ s). For the magnetic field, we are interested in how the field changes after the dipolarization compared to before it, so we define $\delta\mathbf{B}$, the background-subtracted, detrended magnetic field. To construct $\delta\mathbf{B}$, we first remove the effects of the spacecraft's motion through Mercury's dipole magnetic field after which we subtract the average magnetic field over $-20 < t < -10$ s. Using the same spatial gridding as in Figure 3, we examine the superposed epoch profiles of dipolarizations in the new (t, δB_z) coordinates as a function of equatorial location.

The average δB_z over $15 < t < 30$ s from each spatially resolved superposed dipolarization profile is shown in Figure 5a, while Figures 5b and 5c show two example profiles, one tailward and one planetward of the $\beta = 1$ contour, respectively. Tailward of $\beta = 1$, dipolarizations do not exhibit large, prolonged enhancements of the magnetic field following the initial dipolarization. In Figure 5b, for example, the magnetic field decreases slightly prior to the sharp, step-like increase of the dipolarization front (centered at $t = 0$) after which the northward component of the magnetic field remains enhanced for several seconds before falling to near pre-dipolarization values. The average δB_z over $15 < t < 30$ s remains close to within uncertainty of the value over $-20 < t < -10$ s. Correspondingly, the average δB_z over $15 < t < 30$ s for regions tailward of $\beta = 1$ in Figure 5a is small, $\lesssim$5 nT. In contrast, dipolarizations at and planetward of $\beta = 1$ display substantial, prolonged increases in the magnetic field. The superposed dipolarization profile in Figure 5c, for example, shares similar features as the profile in Figure 5b, however, after the initial dipolarization front the magnetic field remains enhanced by ~25 nT for a substantial duration of time (i.e., greater than the typical dipolarizing flux bundle duration of ~10 s, see Dewey, Slavin, et al., 2017). Correspondingly, the average

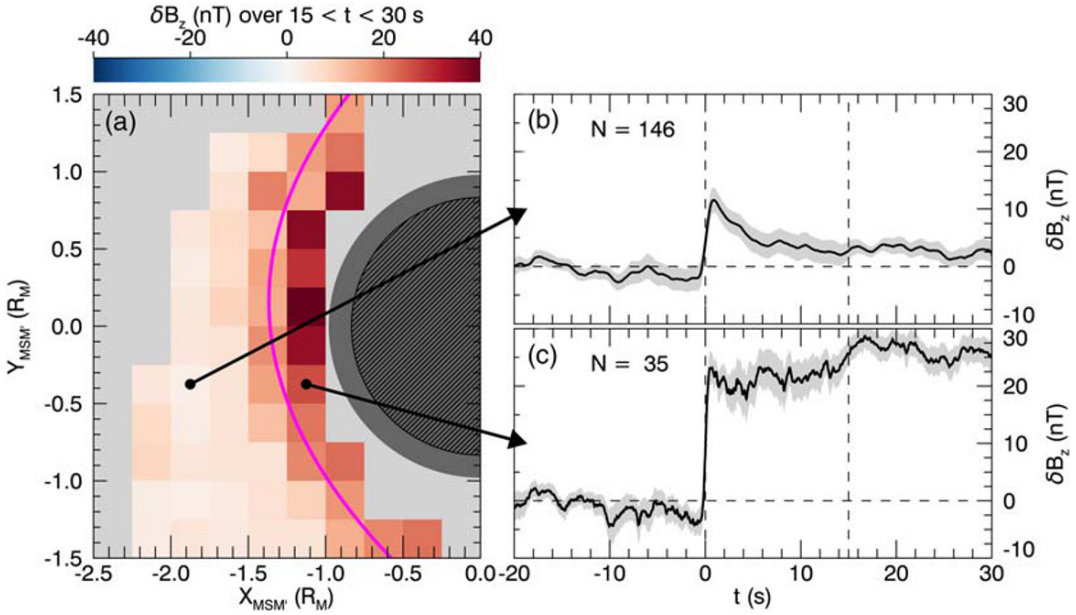

Figure 5. (a) Equatorial distribution of the average detrended, background-subtracted northward magnetic field component (δB_z) following dipolarizations in the same format as Figure 3. The color bar indicates the average δB_z of the superposed dipolarization profiles over $15 < t < 30$ s. Light gray regions have insufficient number of dipolarizations for statistical analysis (<15 dipolarizations, see Figure 3d). The black arrows indicate corresponding spatial locations in (a) for the two example profiles in (b) and (c). For (b) and (c), the thick black line indicates the mean δB_z over the N-dipolarizations at each time step and the light gray indicates the standard error. The vertical dashed lines correspond to $t = 0$ s (the midpoint of dipolarization fronts that the profiles are organized by) and $t = 15$ s. The horizontal dashed lines correspond to 0 nT.

post-dipolarization δB_z at and planetward of the $\beta = 1$ contour in Figure 5a has values ~10–40 nT, with a median value of 29 nT. Planetward of $\beta = 1$, the post-dipolarization δB_z is asymmetric about local midnight with greater strength premidnight (~36 nT) than postmidnight (~26 nT). Synoptically, the prolonged δB_z enhancement planetward of $\beta = 1$ appears to be a large-scale dipolarization of Mercury's near-tail region.

These spatially resolved superposed dipolarization profiles indicate flux pileup occurs in Mercury's magnetotail alongside flow braking. Tailward of $\beta = 1$, superposed dipolarization profiles exhibit only transient increases in the magnetic field consistent with dipolarizations traveling rapidly sunward and passing quickly over the spacecraft and resulting in a small δB_z over $15 < t < 30$ s. Planetward of $\beta = 1$, coincident with where substantial braking occurs, the superposed dipolarization profiles indicate a more permanent increase in the magnetic field with magnetic flux pileup resulting in a large average δB_z over $15 < t < 30$ s. To determine if the synoptic pileup (i.e., large-scale dipolarization) signature across Mercury's near-tail region is physical, we turn to magnetic flux budget analysis in section 3.3 and examine a case study in section 3.4.

3.3. Flux Budget of Statistical Pileup Signature

To determine if the statistical, synoptic flux pileup signature (i.e., large-scale dipolarization) is physical, we first look to determine if dipolarizations could supply sufficient magnetic flux to establish it. We integrate δB_z in Figure 5a planetward of $\beta = 1$ and within $|Y_{MSM'}| < 1.25\ R_M$ to estimate that the large-scale flux pileup contains 0.28 ± 0.08 MWb of magnetic flux. We wish to determine if it is possible for dipolarizations to supply this flux to the inner magnetotail.

The typical magnetic flux transported by a dipolarization can be estimated by

$$\Phi \approx 2\Delta Y V_x \int B_z \, dt$$

where ΔY is the half-width of the dipolarization, assumed to be approximately constant. We can use superposed dipolarization profiles and typical dipolarization flows to estimate these terms, however, the

cross-tail half-width remains unknown. Determining the width of dipolarizations is challenging, even when multispacecraft observations are available (e.g., Nakamura et al., 2004; Sergeev et al., 1996). However, taking advantage of our expanded dipolarization event list, we can employ statistical techniques to provide some insight into their cross-tail width. Similar to determining dipolarization flows, we will not be able to determine the cross-tail width of dipolarizations on an event-by-event basis, but rather, we can use the following statistical analysis to determine a representative value.

Dipolarizations possess several current structures (e.g., Sun et al., 2013). At the dipolarization front, a dawn-to-dusk current separates the surrounding plasma from the enhanced B_z within the dipolarization. While some of this current closes about the dipolarization, most is expected to close as field-aligned currents of the Region-2 sense (e.g., Birn et al., 2019). These field-aligned currents produce perturbations in the magnetic field that we can use to determine if the spacecraft observed the local dawn or dusk flank of the dipolarization. For example, for spacecraft observations of the local dawn side of dipolarizations whose field-aligned current closes into the northern hemisphere, we expect a negative-then-positive perturbation in B_y (i.e., $\delta B_y < 0$ followed by $\delta B_y > 0$) at the dipolarization front. By examining the distribution of where the spacecraft observed the local dawn versus local dusk sides of dipolarizations, we can determine the characteristic cross-tail width. For example, consider if dipolarizations at Mercury typically encompass the entire width of the magnetotail ($-2 < Y_{\mathrm{MSM}'} < 2\ R_{\mathrm{M}}$). Observing the local dawnside would only occur when the spacecraft is postmidnight ($Y_{\mathrm{MSM}'} < 0$), and observing the local duskside would only occur when the spacecraft is premidnight ($Y_{\mathrm{MSM}'} > 0$). The typical separation between observations of local dawn (on average, $Y_{\mathrm{MSM}'} \approx -1\ R_{\mathrm{M}}$) and of local dusk (on average, $Y_{\mathrm{MSM}'} \approx 1\ R_{\mathrm{M}}$) would be $2\ R_{\mathrm{M}}$, the half-width of the full structure ($4\ R_{\mathrm{M}}$).

We implement this methodology to determine the typical dipolarization half-width ΔY in Figure 6. We select dipolarizations in the $\beta > 1$ region (to avoid contamination from braking dipolarizations) that possess significant bipolar signatures in δB_y at the dipolarization front. We use the polarity of the δB_y signature and the spacecraft's $Z_{\mathrm{MSM}'}$ location to estimate if the spacecraft observed the local dawn or local dusk side of the event. A total of 815 dipolarizations met these criteria, with the spacecraft observing local dawn for 450 of these events and local dusk for the remaining 365. The top panels of Figure 6 display the superposed epoch δB_z and δB_y profiles of these events. We invert the sign of δB_y for events when $Z_{\mathrm{MSM}'} < 0$ to produce clear signals in the superposed δB_y profiles (i.e., for events with $Z_{\mathrm{MSM}'} < 0$, we display $-\delta B_y$ in Figure 6). The profiles look nearly identical in magnitude and timing, with just the polarity of the δB_y bipolar signature reversed. The bottom panel displays the cumulative distribution function of the spacecraft's $Y_{\mathrm{MSM}'}$ position for both local dawn (black) and local dusk (red) observations. As expected, the spacecraft position is systematically shifted to greater $Y_{\mathrm{MSM}'}$ when it observed dipolarizations' local dusk side. The separation between the two distribution functions indicates the typical dipolarization half-width. To avoid outliers, we use the 25th to 75th percentiles (dashed vertical lines) to estimate $\Delta Y = 0.15 \pm 0.04\ R_{\mathrm{M}}$. We combine the dipolarization half-width with the Figure 6a B_z profiles and the average downtail V_x flow (192 ± 44 km/s; the horizontal dashed line in Figure 4a) to estimate that a single dipolarization typically transports 0.053 ± 0.019 MWb.

To supply the magnetic flux observed in the flux pileup region would therefore require 5 ± 2 dipolarizations. The number of dipolarizations required to build the flux pileup signature is supported observationally, shown in Figure 7. Figure 7a displays the number of dipolarizations identified during an orbit versus the median time between those dipolarizations (time between successive dipolarization fronts). We include the time between dipolarizations as it suggests a causal link; dipolarizations separated by >2–3 min, for instance, may not be considered to be of the same substorm. Figure 7b shows the marginal distribution of the number of dipolarizations observed per orbit, while Figure 7c shows the time between individual dipolarization fronts (as opposed to the median separation time per orbit in Figure 7a). From Figure 7b, nearly half of orbits (818/1,946 ~ 0.4) contain no dipolarizations. Of the remaining orbits, more orbits contain more than one dipolarization than a single dipolarization. Approximately 18% of all orbits (345/1,946) contain five or more dipolarizations, with the most extreme containing 32. Examining the time between dipolarizations (Figure 7c), most dipolarizations are observed in series with one followed soon by another. The typical time between dipolarization fronts is between 5–20 s while the typical dipolarization duration is ~10 s (Dewey, Slavin, et al., 2017). Combining these distributions together in Figure 7a, only ~6% of orbits contain a sufficient number of dipolarizations (≥5) with median time between dipolarizations <20 s. While this is a small

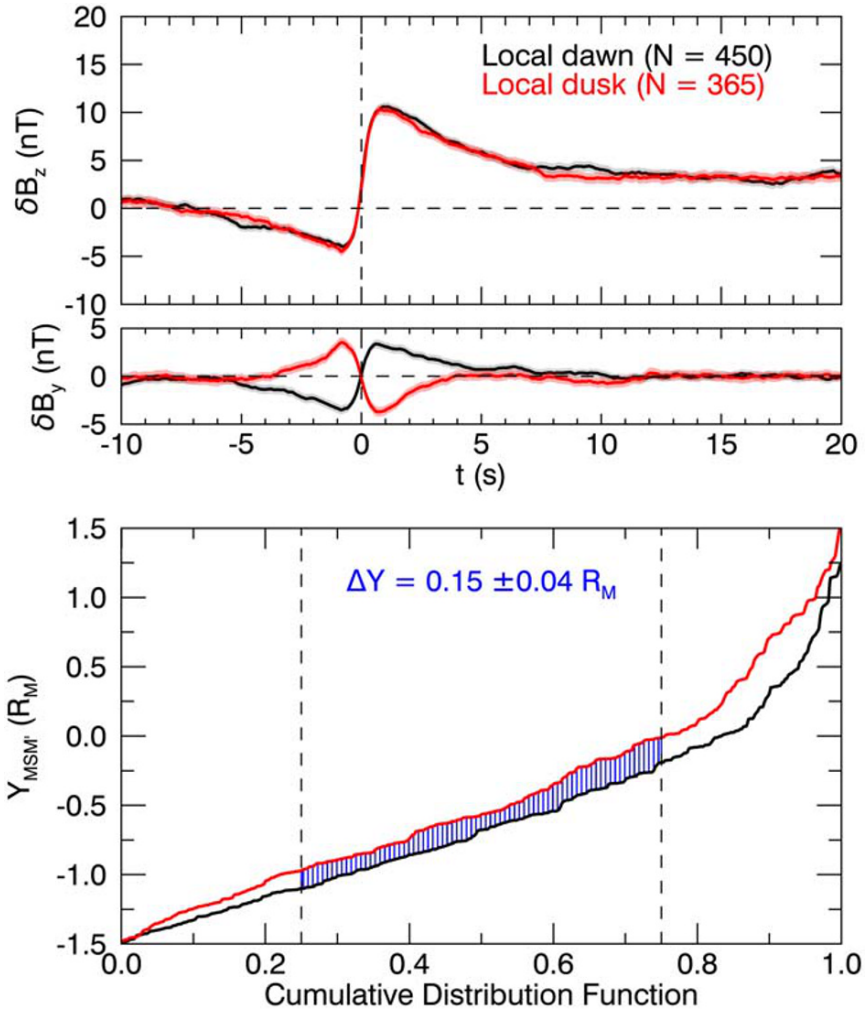

Figure 6. (top) Superposed dipolarization profiles of δB_z and δB_y for dipolarizations observed at their local dawn (black) and local dusk (red) sides in the same format as Figures 5b and 5c. (bottom) Cumulative distribution function of the spacecraft $Y_{MSM'}$ location when it encountered a dipolarization on the dipolarization's local dawn (black) or local dusk (red) side. The separation between the curves (vertical blues lines) indicates the typical cross-tail half-width of dipolarizations. The dashed vertical black lines indicate the 25th and 75th percentiles.

fraction of orbits, this determination is sensitive to the number of active reconnection sites in Mercury's magnetotail (e.g., if two reconnection sites are active we may require the spacecraft to observe 2–3 dipolarizations for the orbit to qualify). We do not intend this fraction of orbits to communicate how common large-scale pileup may occur but rather that the flux pileup signature identified statistically in Figure 5 is indeed possible to establish via multiple dipolarizations.

3.4. Flow Braking and Flux Pileup Example

Thus far, our investigation into flow braking and flux pileup at Mercury has been statistical in focus. To ground these statistical results, we conclude this section by presenting an example of flow braking and flux pileup in Mercury's magnetotail, demonstrating that the statistical results described above are representative of Mercury's magnetosphere. Figure 8 displays MAG and FIPS observations on 7 October 2014 from 18:17:00 to 18:20:00. During this interval, the spacecraft was located in Mercury's postmidnight magnetotail ($Y_{MSM'} = -0.33\ R_M$) close to Mercury's nightside surface (altitude of ~700 km). At these coordinates, we expect the spacecraft to be within the typical braking region identified in section 3.1. The spacecraft crossed Mercury's central current sheet, as evidenced by the change in sign of both B_x and $Z_{MSM'}$. During this

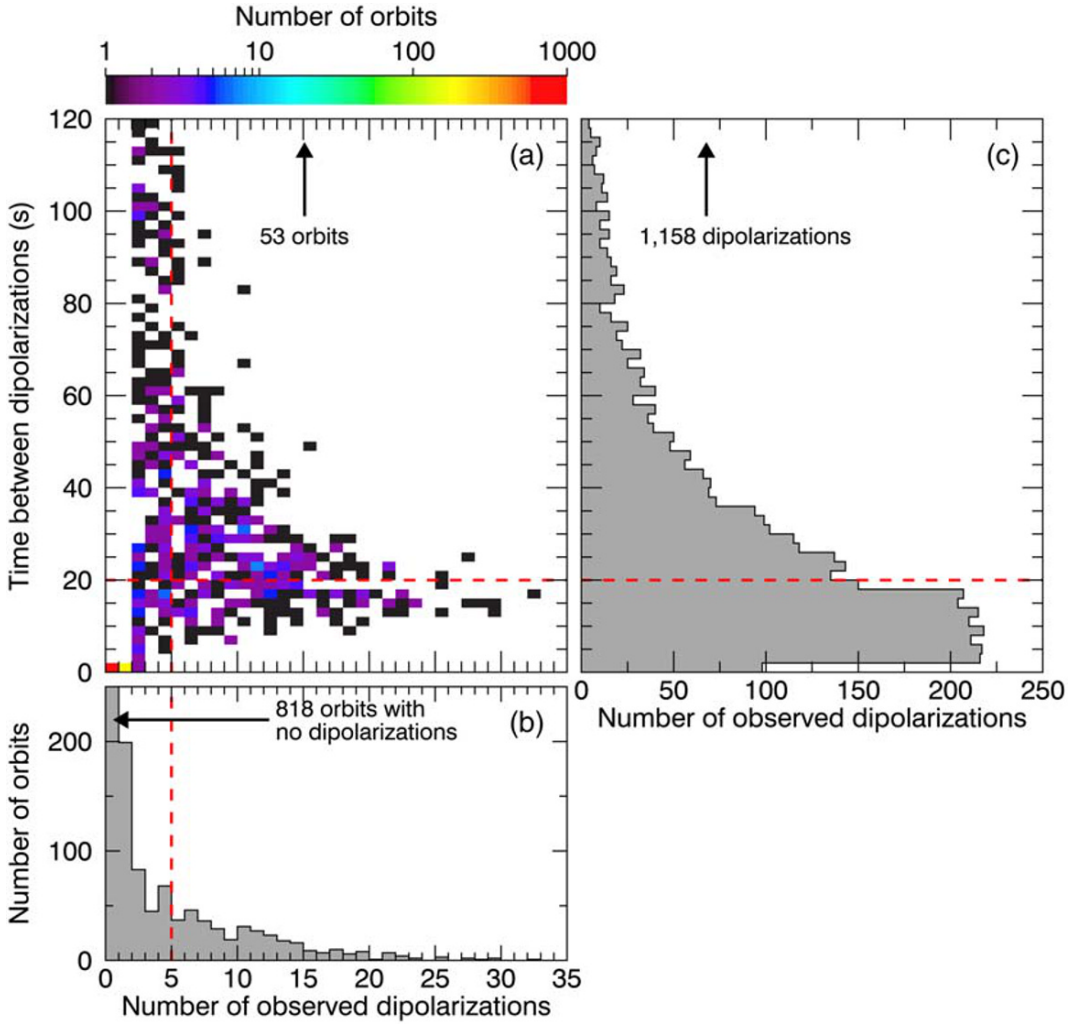

Figure 7. (a) Distribution of the number of dipolarizations observed per orbit versus the median time between dipolarizations during that orbit, where the color bar indicates the number of occurrences. White indicates no occurrences. (b) The marginal distribution of the number of dipolarizations per orbit. (c) The distribution of the time between successive dipolarization fronts. The dashed red lines correspond to thresholds discussed in the text. Arrows in (a) and (c) indicate the number of orbits and dipolarizations, respectively, beyond the range of the plot.

crossing, MESSENGER encountered several dipolarizations, marked by vertical red lines, and observed multiple magnetic and plasma signatures of flow braking and flux pileup.

To provide context to the magnetic field signatures observed during this interval, we include the typical magnetic field conditions at the spacecraft's location as shaded gray regions in each of the magnetic field panels. To determine these conditions, for each point in the magnetic field time series within this interval, we select the 10,000 magnetic field measurements taken closest to the spacecraft's current position that do not belong to the current orbit. We perform a weighted average on these measurements, using the squared distance from each measurement to the current spacecraft position as that measurement's weight, and evaluate variance. These statistical magnetic field conditions not only reflect typical or background observations but also reveal effects of the spacecraft's orbit. For example, the crossing of the central current sheet marked by the reversal in B_x agrees well with the statistical magnetic field description, confirming that this crossing is a result of spacecraft motion rather than current sheet motion.

Prior to the arrival of the dipolarizations, the northward component of the magnetic field (B_z) is weak at ~10 nT. At this location, the spacecraft typically observes B_z ~ 70 nT (gray shaded region) indicating that the current sheet is substantially thinned compared to nominal conditions. Each dipolarization increases

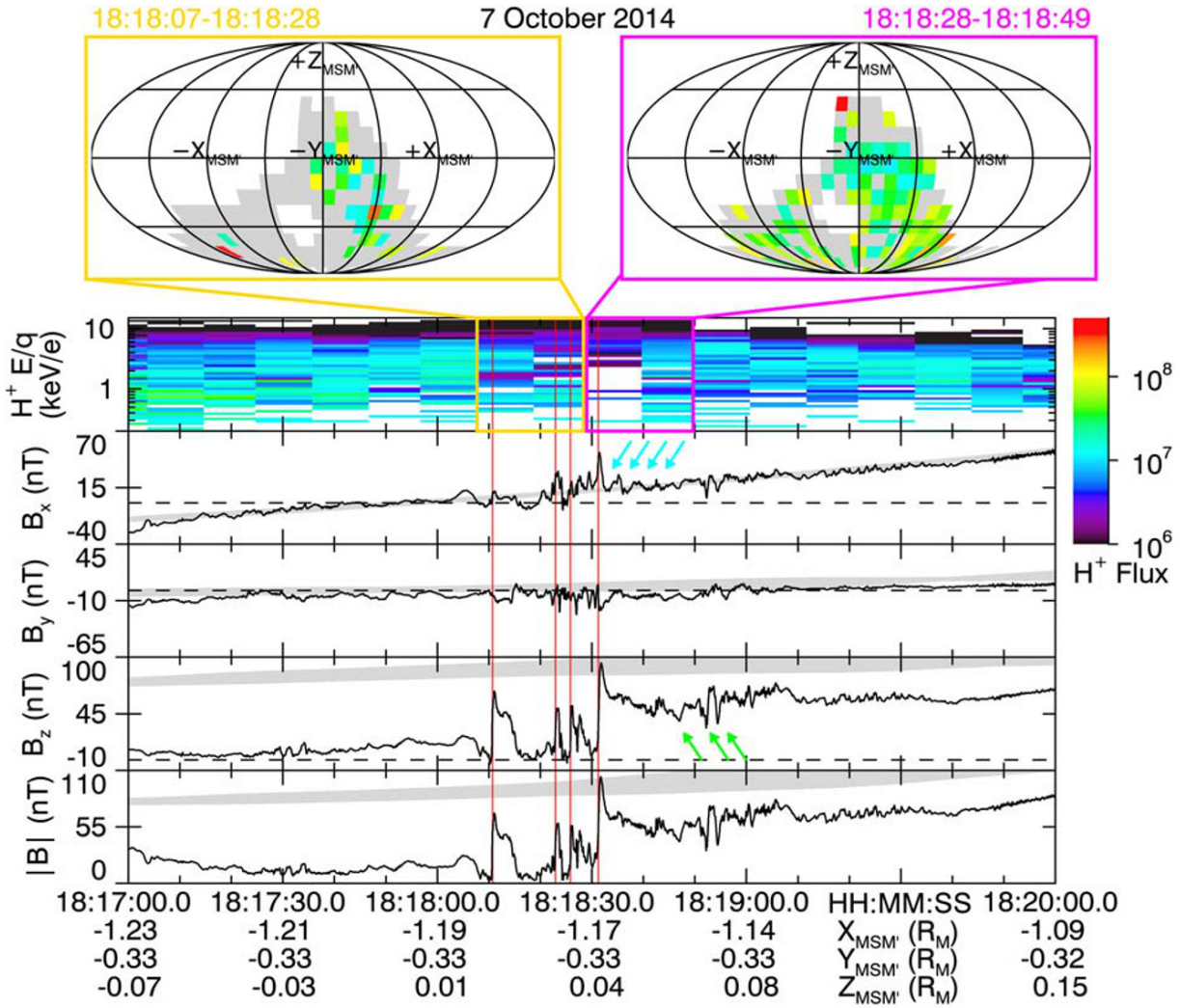

Figure 8. FIPS and MAG observations over 18:17:00 to 18:20:00 on 7 October 2014. The panels from top to bottom are FIPS proton differential flux (values indicated by the color bar, units of s^{-1} cm^{-2} keV^{-1}), B_x, B_y, B_z, and magnetic field strength $|B|$. Below the bottom panel, the time and spacecraft position are listed. The vertical red lines indicate dipolarization fronts as identified by the selection algorithm (see section 2 and Appendix A). The cyan and lime arrows correspond to magnetic fluctuations described in the text. The gray-shaded regions in each magnetic field panel indicate typical magnetic field conditions at this location in Mercury's magnetotail. In the FIPS proton flux spectrogram, the gold and magenta boxed scans correspond to the integrated proton flux maps above the panels. Each flux map indicates the proton flux observed by FIPS as a function of direction in a Mollweide projection. The color bins correspond to the same color bar (units of s^{-1} cm^{-2} sr^{-2}), light gray regions are those within the FIPS field of view but with no observed plasma, and the white regions are those outside the FIPS field of view. Direction labels (e.g., $+X_{MSM'}$) indicate the direction the protons are traveling toward.

the northward component and total field strength, however, the first three dipolarizations represent only transient increases (i.e., local plasma sheet thickening). The dipolarization fronts of the first three dipolarizations increase the northward component (ΔB_z) by 68.2, 38.6, and 45.6 nT over a time of 0.75, 0.45, and 0.45 s, respectively. Although each of these three dipolarizations reach field strengths of ~40–50 nT following their dipolarization fronts, the enhancements are short-lived, with the magnetic field returning to pre-dipolarization values 5.50, 1.65, and 4.55 s after the start of each dipolarization, respectively. The final, and largest, dipolarization is associated with a prolonged enhancement of the magnetic field. The final dipolarization front increases B_z by 83.4 nT over 0.90 s, reaching the statistically-observed B_z for the only time during this interval. The final dipolarization front reaches a local maximum in B_z (95 nT), but unlike the other dipolarizations, the magnetic field does not return to pre-dipolarization values. Instead, B_z remains enhanced at ~55 nT with fluctuations of ±13 nT through the remainder of the interval. This magnetic field is still weaker than what is normally observed at this

location (~100 nT) but is notably enhanced above the field at the beginning of the interval, representing a more permanent dipolarization of the field.

In addition to these B_z signatures, the dipolarizations within this interval are also associated with B_x and B_y perturbations. The first dipolarization is associated with intensification of both B_x and B_y, while the final three dipolarizations display larger-amplitude quasiperiodic fluctuations in both B_x and B_y. These quasi-periodic structures are most readily observed with the third and fourth dipolarizations. Between the third and fourth dipolarizations, the enhancements in B_x last for ~1 s over which B_x changes by ~13 nT. The largest B_x perturbation is associated with the final dipolarization front, with $\Delta B_x = 30$ nT. This large B_x perturbation is associated with a bipolar B_y perturbation, consistent with the structure of an electromagnetic pulse associated with Alfvén waves (e.g., Parks et al., 2007). Following the final dipolarization front, additional fluctuations in B_x and B_y are observed. These perturbations (marked by cyan arrows) are perpendicular to the magnetic field direction, have amplitudes ~6 nT, and period ~3.5 s. Near ~18:18:55, additional fluctuations are observed in the magnetic field (marked by lime arrows), although these are predominately parallel to the magnetic field (primarily along B_z). These perturbations are similar to those analyzed at higher latitudes by Sun et al. (2015). The perpendicular fluctuations following the final dipolarization front are consistent with Alfvén waves while the later parallel fluctuations are consistent with compressional wave modes. Following the interpretation of Sun et al. (2015), these waves are suggestive of flow braking.

To determine if these dipolarizations are associated with bulk plasma flows, we examine FIPS proton flux maps. The two FIPS scans that cover the first three dipolarizations correspond to the gold-boxed flux map, while the scans that cover the final dipolarization correspond to the magenta-boxed flux map. For both ranges, the FIPS field of view is oriented such that it most readily detects protons traveling in $-Y_{\mathrm{MSM}'}$ and $-Z_{\mathrm{MSM}'}$ directions. While the missing regions of velocity space are too large to unambiguously determine flow direction and magnitude, the FIPS scans that cover the first three dipolarizations (18:18:07 to 18:18:28) are suggestive of a sunward flow with more plasma traveling in $+X_{\mathrm{MSM}'}$ than in $-X_{\mathrm{MSM}'}$. In contrast, the final dipolarization does not appear to be associated with a substantial flow, with its flux map (18:18:28 to 18:18:49) appearing substantially more isotropic. The average energy of protons within 45° of $+X_{\mathrm{MSM}'}$ is 11.2 ± 4.6 keV in the first distribution and 3.6 ± 1.3 keV in the second. In contrast, the average energy of protons along all directions in each distribution is 2.8 ± 0.4 and 3.2 ± 0.2 keV, respectively. The energy of protons near $+X_{\mathrm{MSM}'}$ decreases from much greater than the distribution-average energy in the first distribution to within uncertainty of it within the second distribution, consistent with the deceleration of a sunward flow.

Taken together, these magnetic field and plasma observations are indicative of flow braking and flux pileup in Mercury's magnetotail. In the span of ~30 s, the spacecraft observed four dipolarizations. The first three appear associated with sunward flow and pass over the spacecraft, resulting in temporary, transient increases in the magnetic field. The final dipolarization, in contrast, displays no meaningful flow along $X_{\mathrm{MSM}'}$ and is instead associated with a prolonged magnetic field enhancement, characteristic of flow braking and flux pileup. Additionally, perturbations in the magnetic field following the final dipolarization are consistent with Alfvén and compressional waves expected to be associated with flow braking at Mercury (Sun et al., 2015). From the first dipolarization to the last in this time series, the spacecraft moved only 40 km sunward, 3 km duskward, and 60 km northward. For the spacecraft to observe a series of sunward-traveling dipolarizations followed by an approximately stagnant flux pileup region while moving only a small distance in Mercury's magnetotail, it is possible that the final dipolarization may in fact be the piled-up signature of the first three dipolarizations after they experienced intense flow braking.

4. Discussion

Using an algorithm to identify magnetotail dipolarizations in the magnetic field time series, we have presented both statistical and case study evidence for the flow braking and subsequent magnetic flux pileup associated with dipolarizations in Mercury's magnetotail. We find that downtail of the braking region, the frequency of dipolarizations and the typical sunward flow speed of these structures remains approximately constant. As dipolarizations approach Mercury's near-tail region, as indicated by where the proton plasma beta (β) reaches unity, both the frequency and flow speed of dipolarizations decrease substantially. These observations are analogous to the earliest evidence for the existence of a flow-braking region at Earth

(e.g., Shiokawa et al., 1997). While Mercury's braking region is thinner (~500 km) and situated closer to the planet (~900 km in altitude) than Earth's, the intense magnetic pressure gradients at both planets appear responsible for flow braking and deflection. Coincident with the decrease in dipolarization frequency and flow speed, the magnetic pressure gradient in Mercury's near-tail region increases by a factor of 60 ± 20. The proton plasma pressure gradient also increases at this location, but it increases by a more modest factor (16 ± 7).

We find that as these dipolarization flows brake, they accumulate magnetic flux in Mercury's near-tail region. Within the braking region, dipolarizations are associated with prolonged enhancements in the magnetic field, as opposed to transient enhancements observed with dipolarizations traveling quickly over the spacecraft upstream of the braking region. We examine the magnetic flux budget of both this pileup region and of individual dipolarizations to determine that spacecraft observations support these statistical findings. Indeed, although building the synoptic flux pileup signature requires several dipolarizations (5 ± 2), dipolarizations are typically observed in series, such that the spacecraft has observed this number or more of dipolarizations in sequence. More simply, we estimate that the flux pileup region contains 0.28 ± 0.08 MWb. Loading of Mercury's magnetotail increases the magnetic flux content of the lobes by 0.69 ± 0.38 MWb (Imber & Slavin, 2017) so there is sufficient magnetic flux loaded into the magnetotail during a typical substorm at Mercury to develop the flux pileup region (i.e., large-scale dipolarization).

4.1. Westward Expansion of Magnetic Flux Pileup

We find that the synoptic signature of magnetic flux pileup associated with dipolarizations in Mercury's magnetotail exhibits an asymmetry about local midnight, with a stronger dipolarized field premidnight than postmidnight. This asymmetry in pileup is likely related to the asymmetry in dipolarization occurrence and westward expansion of the pileup region. Consistent with previous studies of Mercury's dipolarizations (Dewey et al., 2018; Sun et al., 2016), we find that dipolarizations are more common to Mercury's postmidnight magnetotail as measured both by frequency and by fraction of orbits that possess them. Without the ability to constrain the magnetic flux transported by each dipolarization independently, we interpret the increased rate of dipolarizations postmidnight to indicate that more magnetic flux is usually transported to the postmidnight inner magnetosphere than that premidnight, such that we expect pileup to initiate more commonly postmidnight. If pileup is usually initiated in the postmidnight sector, then its expansion westward into the premidnight sector may be responsible for the statistical pileup signature we observe there. In Figure 3b, the average V_y flow of bins that intersect the $\beta = 1$ contour or are planetward of it is 53 ± 31 km/s, consistent with westward motion about the planet. Westward expansion may explain why there are instances of pileup observed premidnight but it does not immediately explain why the statistical premidnight pileup signature is stronger than that postmidnight.

We hypothesize that two factors may contribute to the pileup strength asymmetry. For bins within the breaking region in Figure 5a, we observe that the postmidnight bins contain a greater average number of dipolarizations (44 ± 7) than the premidnight bins (17 ± 5). Similarly, the standard error in δB_z is greater postmidnight (5.0 ± 0.9 nT) compared to premidnight (2.8 ± 0.5 nT). We interpret the larger number of dipolarizations and the greater variance in the pileup signature postmidnight to indicate that the postmidnight statistical pileup signature may be averaged down by weak or noninstances of pileup. One explanation could be that there is a threshold of pileup above which flux expands premidnight. At Earth, azimuthal expansion occurs after substantial pileup. If this is true for Mercury, then while pileup of all strengths may be observed postmidnight, only sufficiently strong instances of pileup expand westward and can be observed premidnight. In other words, weaker instances of pileup act to dilute the statistical postmidnight pileup signature. A second and similar explanation could be that some dipolarizations within the typical breaking region may not have experienced strong breaking when they are observed by the spacecraft. Such dipolarizations are not expected to produce a pileup signature, so when they are observed in the braking region, they would weaken the statistical pileup signature there. For example, the case study examined in section 3.4 contains four dipolarizations, only the last of which exhibits pileup. The four dipolarizations map to the same bin in Figure 5a so the first three dipolarizations dilute the pileup signature of the fourth. These two factors have different physical mechanisms but the same implication: the premidnight pileup signature is biased by stronger, less frequent instances of pileup resulting from westward expansion while the postmidnight signature is

averaged down by weak or non-pileup events. Future investigations into this topic at Mercury will be of particular value in addressing the degree to which these mechanisms explain the asymmetry in pileup.

4.2. Substorm Current Wedge Formation

At Earth, flux pileup is associated with the substorm current wedge: Could a current wedge exist at Mercury? Without ground magnetometers or multi-point spacecraft observations, it may be difficult to determine unambiguously. However, the results described in section 3 suggest it may be possible, if not common, to Mercury's substorms. Alfvén waves, and the field-aligned currents they carry, communicate motion of magnetic field lines of the magnetosphere to the inner conducting boundary in which they are rooted (Southwood & Kivelson, 1991). For Earth, this boundary is the ionosphere, while at Mercury, it is its large conducting core. For a static field-aligned current system like the substorm current wedge to establish, it requires multiple bounces of the current-carrying Alfvén waves (see, e.g., Kepko, McPherron, et al., 2015). At Mercury's braking region, we find a typical Alfvén speed of ~1,000 km/s (see Figure 4d). We estimate, by assuming dipole field line geometry, that field lines are ~2 R_M in length above Mercury's conducting core at local midnight within the braking region. For such locations close to the planet, the assumption of dipole field line geometry is expected to be valid (see, e.g., Rong et al., 2018). To execute a complete round-trip bounce would therefore require ~10 s for an Alfvén wave assuming the Alfvén speed remains constant along the field line. If we assume the magnetic field strength along the field line scales like that of a dipole field line, then the round-trip time would be ~6 s. The typical substorm unloading time at Mercury is ~100 s (Imber & Slavin, 2017), allowing for many bounces of Alfvén waves within the braking region.

Although the typical substorm unloading duration allows for many (~10–16) bounces of Alfvén waves to attempt to establish a static current system, the resistive regolith that covers Mercury's conductive core presents additional restraints on establishing a current wedge. To communicate with the core, the skin depth of the Alfvén wave must be greater than the depth of the regolith. With a period of ~6–10 s and a height-integrated regolith conductivity of ~1 siemen (Anderson et al., 2014), the skin depth of these Alfvén waves would be between 750–960 km, which is greater than the regolith layer (~400 km). While these Alfvén waves reach the conductive core, their passage through the resistive regolith reduces their current density. In a round-trip bounce, the waves pass through an accumulated ~1,600 km of regolith, such that the amplitude (i.e., current density) of the waves after a complete bounce would only be ~12–19% the initial value. Therefore, while a single Alfvén wave within the braking region may complete a sufficient number of bounces during a typical substorm unloading to establish a static field-aligned current system, the resulting current density would be negligible. Furthermore, while the bounce time is substantially smaller than the substorm unloading time at Mercury, it is on the similar timescale as an individual dipolarization. As observed by dipolarizations passing over the spacecraft, the transient increase in the magnetic field associated with individual dipolarizations last for ~10 s (see Dewey, Slavin, et al., 2017 and Figure 5b above). Dipolarizations are expected to interact with the braking region for about this duration as well. This timescale allows for only ~1–2 round-trip bounces of an Alfvén wave, an insufficient number to prevent the dipolarization structure from dissipating. Both the damping of Alfvén waves and the dissipation of an individual dipolarization structure before a static field-aligned system can be established point toward a common solution: continuous supply of dipolarizations.

When observed, dipolarizations are more commonly observed in series with other dipolarizations than as isolated events (see Figure 7b). A series of dipolarizations, one after another, would supply new Alfvén waves to the braking region (e.g., Sun et al., 2015 and section 3.4 above) and allow existing Alfvén waves to maintain the magnetic shear about incoming dipolarizations that separate them from the surrounding plasma (i.e., prevent dissipation). Indeed, from flux budget analysis of a typical dipolarization compared with the flux loaded into the magnetotail (Imber & Slavin, 2017), we expect multiple (13 ± 9) dipolarizations during a substorm unloading phase. With most dipolarizations observed ~5–20 s apart (Figure 7c), these dipolarizations would arrive at the braking region within 1–2 Alfvén bounce times of another. Therefore, despite the limitations imposed by the conducing core, the resistive regolith, and the Alfvén bounce times, observations of dipolarizations at Mercury suggest a current wedge structure appears possible to form in Mercury's magnetotail. With the expectation that such a current wedge at Mercury would require the interaction between the field-aligned current systems (i.e., Alfvén waves) of multiple, successive dipolarizations, it is surprisingly similar to the “wedgelet” conceptual model of Earth's substorm current wedge.

With the formation of a current wedge possible at Mercury, we determine its characteristics by examining the synoptic flux pileup signature (i.e., large-scale dipolarization) of Figure 5. Using a simple current wedge line model (e.g., Poh et al., 2017b), we estimate that the current consistent with this enhanced δB_z would need to be ~14.6 ± 5.0 kA in the plasma sheet. This current is ~20 times weaker than that at Earth (e.g., Birn et al., 2019; Kepko, McPherron, et al., 2015). From the weak sunward flow in the braking region (~50–100 km/s), we estimate that the potential drop across the current wedge in the equatorial plane would be ~12.2 ± 3.4 kV, indicating a height-integrated electrical conductance of ~0.8 ± 0.4 siemens, which is consistent with recent estimates from Mercury's Region-1 static current system (Anderson et al., 2014).

4.3. Core Induction and Surface Precipitation

The substorm current wedge may not be the only means by which dipolarizations and the magnetotail couple to Mercury's conducting core. Mercury's core responds to compression of the magnetosphere by inducing currents on its surface to resist these changes. The topic of induction has been most thoroughly studied with regard to changes in solar wind dynamic pressure (e.g., Jia et al., 2015, 2019; Johnson et al., 2016; Slavin et al., 2014; Zhong et al., 2015) but studies of Mercury's magnetotail have also discussed the possibility of inducing currents on the core's nightside surface in response to compression of the planet's nightside inner magnetosphere (e.g., Dewey et al., 2018). Based on our findings, we expect that dipolarizations are unlikely to elicit a strong inductive response from the planetary core. Dipolarizations provide only small increases in dynamic pressure with which to compress Mercury's nightside magnetic field. Given the characteristics of dipolarizations described in section 3 and by Dewey et al. (2018), the typical dynamic pressure of a dipolarization is of order ~0.1 nPa. Mercury's inner magnetosphere has magnetic pressure of order ~5 nPa (see Figure 4) so individual dipolarizations are unlikely to substantially compress the nightside inner magnetosphere and generate inductive currents on the core. By comparison, changes in solar wind dynamic pressure along Mercury's highly eccentric orbit (~11 nPa at aphelion to ~26 nPa at perihelion, Slavin & Holzer, 1981) result in induction currents that change Mercury's magnetic moment by only ~5% (Johnson et al., 2016). To reach similar dynamic pressures in Mercury's magnetotail, dipolarizations would need to be associated with extreme density (>5 cm^{-3}) and flow speeds (>1,000 km/s). Even then, dipolarizations are localized in cross-tail extent so they would only compress the nightside inner magnetosphere regionally. Increases in solar wind dynamic pressure compress the dayside magnetosphere globally so any nightside inductive currents would be much smaller in spatial extent on the core than the dayside equivalents.

Dipolarizations also interact with Mercury's surface. There is some evidence that a small fraction of dipolarizations may reach Mercury's low-latitude nightside surface. The occurrence maps of dipolarizations (Figure 2) indicate that some dipolarizations are observed at <200 km altitude. Furthermore, organizing dipolarization frequency about $\beta = 1$ (Figure 4) indicates that far downstream of the braking region (e.g., $\Delta X_{MSM'} = 0.5\ R_M$) dipolarizations are still observed even if at a low rate. At these locations, the rate of dipolarizations (~0.1–0.2 min^{-1}) is much lower than the downtail occurrence (~0.6 min^{-1}) implying that no more than ~10–20% of dipolarizations travel far beyond the braking region. At the flanks of the magnetotail, dipolarizations traveling this far beyond $\beta = 1$ may return their magnetic flux to the dayside directly, while those behind the planet may impact the low-latitude surface (or approach within a gyroradius of the surface). As most precipitation in Mercury's plasma sheet is expected at middle or high latitudes (e.g., Korth et al., 2014), the opportunity for dipolarizations to transport plasma and magnetic flux directly to the low-latitude surface may have consequences for exospheric generation and space weathering (e.g., Raines et al., 2016). Aside from dipolarizations reaching the low-latitude nightside surface, the close proximity of the braking region to the planet's surface (altitude of ~900 km) results in large expected loss cones (~25–40°) such that substantial plasma precipitation may occur with most dipolarizations in the braking region already. The mass transport from dipolarizations in Mercury's magnetotail deserves further dedicated study.

5. Conclusions

We present strong evidence for flow braking and magnetic flux pileup associated with dipolarizations in Mercury's magnetotail. We summarize our findings in Figure 9, a schematic representation of flow braking, flux pileup, and current wedge formation. Dipolarizations first begin in the midtail as a product of reconnection and are transported sunward by the fast reconnection outflows. As dipolarizations and their associated flows approach Mercury's inner magnetosphere, the flows encounter steep magnetic pressure gradients from

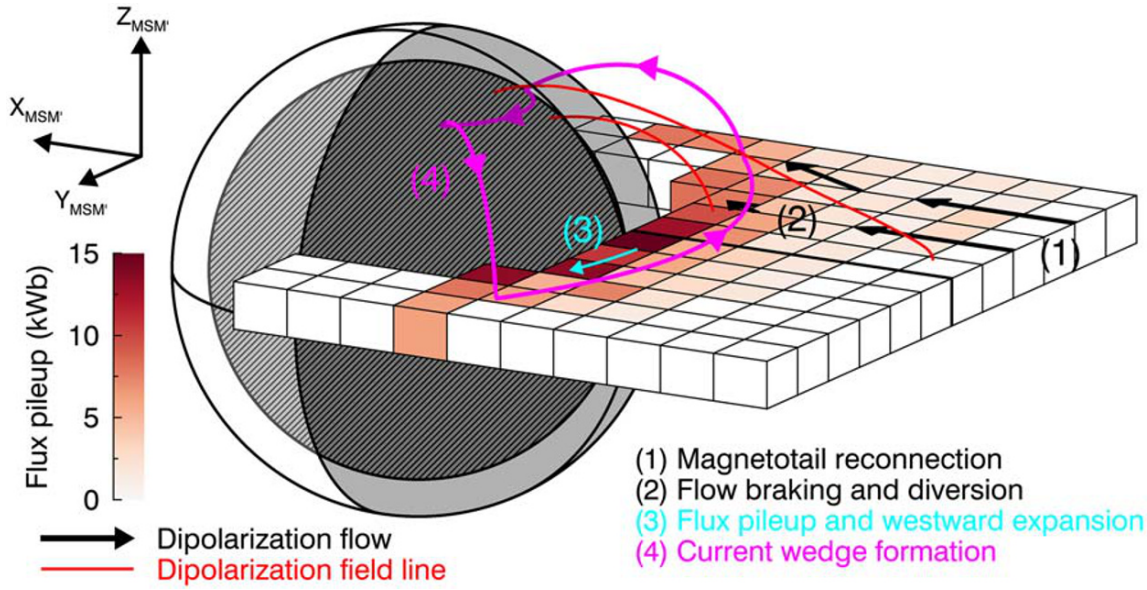

Figure 9. Schematic of flow braking, flux pileup, and current wedge formation from dipolarizations within Mercury's magnetotail. The colored boxes are the pileup observations from Figure 5. Features are at accurate scaling with respect to each other.

Mercury's planetary dipole field, causing the flows to brake and deflect. A small fraction (no more than ~10–20%) of dipolarizations may be able to reach the dayside magnetosphere or Mercury's nightside surface while the remainder typically brake within a region ~500 km in thickness located ~900 km in altitude above Mercury's local midnight surface as evidenced by substantial and significant decreases in dipolarization frequency and sunward flow speed. As dipolarizations brake, their transported magnetic flux accumulates. Current-carrying Alfvén waves generated by the motion and braking of the dipolarization field lines communicate these changes to Mercury's conductive core. As additional dipolarizations brake and pileup, the large-scale dipolarization near the inner magnetosphere expands westward into the premidnight magnetotail. Simultaneously, the interaction of the Alfvén waves from the braking of multiple, continuous dipolarizations may be able to establish a large-scale current system to support the enhanced magnetic field within the pileup region, akin to Earth's substorm current wedge. Despite the differences between Mercury and Earth's magnetospheres, namely the smaller spatiotemporal scales, enhanced effects of magnetic reconnection, and lack of ionosphere at Mercury, the dynamics of dipolarizations are surprisingly similar. While we have presented both statistical analysis and a case study in support of our conclusions, observations from the en route BepiColombo spacecraft mission and global modeling simulations of Mercury's magnetosphere will be of particular value to continue to investigate and constrain these results.

Appendix A: Dipolarization Identification Algorithm

The dipolarization identification technique is described briefly in section 2. In this appendix, we describe the procedure in greater detail. Previous approaches to determining dipolarizations via autonomous algorithms have focused on identifying the leading edge of the event (dipolarization front) using a sliding window (e.g., Liu et al., 2013; Sun et al., 2016). We follow a similar, but modified, approach by first identifying potential dipolarization fronts within the magnetic field time series and then applying a series of physical tests to determine if these signals represent dipolarizations. We take advantage of the initial statistical characterization of dipolarizations at Mercury from Sundberg et al. (2012), Sun et al. (2016), and Dewey, Slavin, et al. (2017) to set several empirical limits in identifying events.

To identify potential dipolarization fronts, we examine each point in the $B_z(t)$ time series for a strong, local, coherent, positive gradient. At point i in the time series (i.e., $t = t_i$), we determine the minimum time (Δt) by which B_z increases by ΔB_z, i.e., $B_z(t_i+\Delta t) = B_z(t_i)+\Delta B_z$. The parameter ΔB_z will therefore be the minimum increase in B_z of an identified dipolarization front. We use $\Delta B_z = 10$ nT, which corresponds the 5th

percentile of dipolarization front ΔB_z identified by Dewey, Slavin, et al. (2017). In other words, 95% of dipolarizations identified by Dewey, Slavin, et al. (2017) have dipolarization front $\Delta B_z > 10$ nT. For the interval of t_i to $t_i + \Delta t$ to qualify as a potential dipolarization front, we require

1. $\Delta B_z/\Delta t \geq 5$ nT/s;
2. minimum$(B_z(t_i < t < t_i{+}\Delta t)) \geq B_z(t_i)$; and
3. $\mu(\delta B_z(t_i < t < t_i + \Delta t)) > \sigma(\delta B_z(t_i < t < t_i + \Delta t))$

where $\delta B_z(t)$ is the point-to-point change in $B_z(t)$, μ is the mean function, and σ is the standard deviation function. The first criterion requires local gradients to be both strong and positive, while the last two criteria require local gradients to be coherent. We set the threshold of the first criterion empirically by examining dipolarizations of Dewey, Slavin, et al. (2017), the distribution of $\Delta B_z(\Delta t)$ across the 1,946 dipolarization-search intervals, and to avoid misinterpreting the spacecraft's motion through the current sheet (or the current sheet's motion over the spacecraft) as a potential event. Each group of sequential points in the time series that meet these three criteria is determined to be potential dipolarization front. We require that each potential dipolarization front have a minimum duration of 0.4 s (eight or more sequential MAG observations) to ensure the dipolarization front is well resolved. For comparison, Dewey, Slavin, et al. (2017) found a minimum dipolarization front duration of 0.7 s.

To determine if a potential dipolarization front corresponds to a dipolarization or not, a series of tests is applied. These tests include physical and statistical considerations and are designed to mimic signals that one's eye would use to select dipolarizations and to avoid false-positives from other magnetotail phenomena, such as flux ropes, tail flapping, and magnetospheric waves Because the duration of dipolarization fronts can vary substantially (i.e., from <1 to >5 s, see Dewey, Slavin, et al., 2017), these tests use time durations standardized by the potential dipolarization front's duration Δt_{DF}. The first test evaluates if the increase in B_z across the potential dipolarization front is meaningful compared to the fluctuations in the magnetic field that surround it:

$$\frac{\mu(B_z(t_2<t<t_2+\gamma\Delta t_{\mathrm{DF}})) - \mu(B_z(t_1-\alpha\Delta t_{\mathrm{DF}}<t<t_1))}{\sqrt{\sigma(B_z(t_2<t<t_2+\gamma\Delta t_{\mathrm{DF}}))^2 + \sigma(B_z(t_1-\alpha\Delta t_{\mathrm{DF}}<t<t_1))^2}} > \eta$$

where t_1 is the start time of the potential dipolarization front, t_2 is the end time of the potential dipolarization front, and therefore $\Delta t_{\mathrm{DF}} = t_2 - t_1$. The parameters α, γ, and η are determined from optimization, described below. The second test evaluates if the potential dipolarization has sufficient duration:

$$\tau_2 > \varepsilon\Delta t_{\mathrm{DF}}$$

where

$$\tau_2 = t(B_z = \widetilde{\mu}(B_z(t_1<t<t_2)); t > t_2) - t_2$$

and $\widetilde{\mu}$ is the median function. The parameter τ_2 reflects the duration of time following the end of the potential dipolarization front that B_z is elevated above the median B_z during the potential front. The parameter ε is determined from optimization. The third test evaluates if the potential dipolarization stands above the preceding magnetic field for sufficient time:

$$t_1 - t_0 - \tau_1 > \zeta\Delta t_{\mathrm{DF}}$$

where

$$\int_{t_0}^{t_1} \lambda(t)\, \mathrm{d}t = \tau_1$$

and

$$\lambda(t) = \begin{cases} 1 \text{ for } B_z(t) \geq \widetilde{\mu}(B_z(t_1<t<t_2)) \\ 0 \text{ for } B_z(t) < \widetilde{\mu}(B_z(t_1<t<t_2)) \end{cases}$$

and ζ is determined from optimization. This third test is similar to the second in that it determines the duration of time before the potential dipolarization front that the magnetic field was below the median level during the potential front, but with the addition that it allows for short intervals of time (relative to the duration of the potential dipolarization) that the field was above the median level. We find that dipolarizations often occur in series with other dipolarizations (e.g., see Figure 7 within section 3.3 or Figure 2 of Sundberg et al., 2012) and that without allowing for an interval of B_z greater than the median level, many dipolarizations in series would be disqualified. The final test evaluates how the change in B_z across the dipolarization front compares in magnitude to the preceding field:

$$\frac{B_z(t_2) - B_z(t_1)}{\mu(B_z(t_1 - \zeta\Delta t_{\mathrm{DF}} < t < t_1))} > \nu$$

where ν is determined by optimization. We experimented with additional tests and tests with different functional forms, and found that these four tests provide the minimum yet sufficient criteria to determine which potential dipolarization fronts indeed correspond to dipolarizations.

To optimize the six (α, γ, η, ε, ζ, and ν) free parameters, we developed a training set of dipolarizations to determine algorithm performance. We selected, at random, 196 of the 1,946 intervals (~10%) and for each potential dipolarization front within these selected intervals, evaluated by eye whether it corresponds to a dipolarization. The 196 intervals contain 1,775 potential dipolarization fronts, of which 623 correspond to dipolarizations and 1,152 do not. By systematically varying the six free parameters, we evaluated algorithm performance on this training set. We follow the optimization technique outlined by Azari et al. (2018), which focuses on the Heidke Skill Score (HSS) for evaluating and optimizing algorithm performance. HSS ranges from $-\infty$ (perfect antiprediction) to 1 (perfect prediction), with HSS = 0 representing prediction as good as random chance. For a discussion of the advantages of using HSS for identification algorithms in space physics, see Azari et al. (2018), and references therein. For our algorithm, maximizing HSS to determine free parameter values led to a large fraction of false positives identified as events. At the maximum HSS (0.806), 13.0% of events identified by the algorithm to be dipolarizations were false positives, and 7.1% of all 1,152 non-dipolarizations were detected as events. We therefore modified the Azari et al. (2018) approach by limiting the maximum fraction of false positives to 5%. Setting this limit, the maximum qualifying HSS is 0.764, corresponding to following free parameter values.

$$\alpha = 1.75$$
$$\gamma = 1.50$$
$$\eta = 1.75$$
$$\varepsilon = 1$$
$$\zeta = 2$$
$$\nu = 0.3$$

With these parameters, the rate of dipolarization detection is 73.7%, the rate of non-dipolarizations being detected as events is 2.1%, and the fraction of algorithm-identified events that are false positives is 5.0%. The HSS of 0.76 indicates this algorithm identifies dipolarizations much better than random chance. For comparison, semiautonomous identification of injection events at Saturn by Azari et al. (2018) has an HSS of 0.56, while space weather models typically have HSS < 0.5 for predicting magnetic perturbations at ground magnetometer stations (Pulkkinen et al., 2013).

Appendix B: Statistical Flows From Partial FIPS Composite Velocity Space Distributions

To estimate ion bulk flows, we follow the procedure developed by Dewey et al. (2018). We refer readers to that study for technical details of the method and its implementation. Below we present a summary of the method and expand its capabilities to evaluate flows from velocity space distributions less complete than those presented in Dewey et al. (2018).

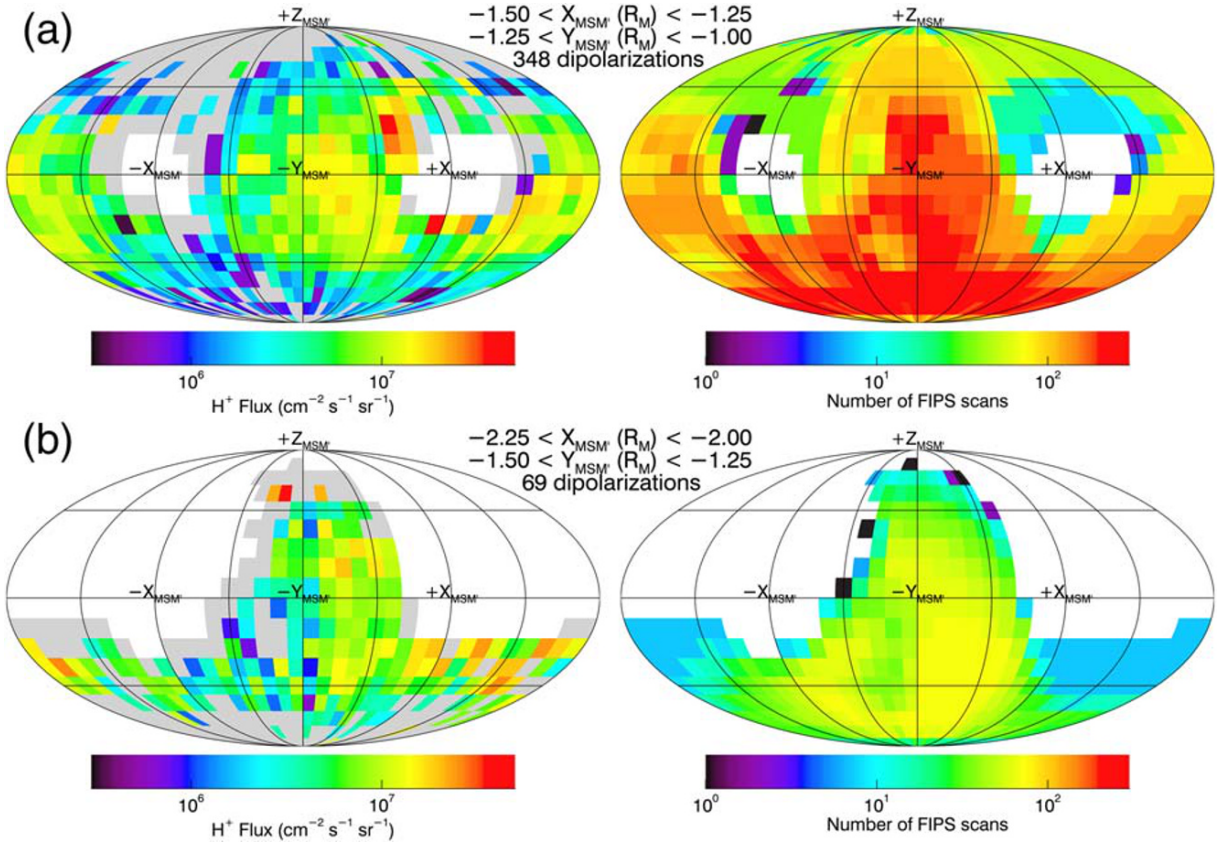

Figure B1. Composite velocity space distributions from FIPS measurements of dipolarizations. (left column of a and b) Proton flux maps, where white are unobserved regions and gray are observed regions that have no measured counts. (right column) Number of FIPS scans that contribute to constructing the proton flux maps for each direction in velocity space. White indicates that no scans observe that direction. The text between the distributions indicates which location of Figure 3 these distributions correspond to as well as the number of dipolarizations used to construct the composite distributions.

FIPS cannot measure complete velocity space distributions at its native time resolution due to limitations imposed by the MESSENGER spacecraft. The spacecraft is three-axis stabilized so FIPS only observes ~1.15π sr of the sky during a single scan. Although the spacecraft does not spin, it does rotate slowly over the course of its orbit (~0.04°/s) to keep the sunshade pointed sunward and to regulate the pointing of remote sensing instruments. This rotation is too slow for FIPS to construct complete velocity space distributions between subsequent scans but it does change the pointing of the FIPS instrument over time. Constructing a complete velocity space distribution therefore requires combining FIPS scans from different intervals. Selecting FIPS observations of similar magnetospheric phenomena (e.g., dipolarizations) allows us to construct a statistical description of velocity space associated with those events from which we can determine bulk flows.

Despite the number of FIPS scans combined to form a composite velocity space distribution, this distribution will not be complete in velocity space. The center of FIPS's field of view (FOV) is approximately perpendicular to the spacecraft's sunshade so FIPS cannot observe to within ~20° of the spacecraft's sunshade axis. The requirement that the sunshade points sunward therefore prevents FIPS from observing within ~20° of $\pm X_{MSM}$. When calculating statistical flows, Dewey et al. (2018) mitigate the effects of missing velocity space regions by comparing the velocity space distribution to that produced by a software model of the FIPS instrument (Dewey, Raines, et al., 2017). In our study, we use fewer FIPS scans on average in constructing composite velocity space distributions, and as a consequence, many of these distributions have larger missing regions than the distributions discussed in Dewey et al. (2018). Figure B1 provides examples of distributions used in determining statistical flows for Figure 3. Figure B1a is a nearly complete distribution similar to that of Dewey et al. (2018) while Figure B1b is less complete.

To determine which velocity components can be reliably determined from these less complete distributions, we define several parameters that quantify how much of velocity space is observed and how symmetric that coverage is. First, we define the FOV distribution $\mathcal{F}(\theta,\phi)$. This distribution has standard spherical coordinates with θ as the zenith angle and ϕ as the azimuth angle. The value of $\mathcal{F}(\theta,\phi)$ is binary: $\mathcal{F}(\theta,\phi)=1$ for velocity space directions observed by one or more FIPS scans and $\mathcal{F}(\theta,\phi)=0$ for unobserved directions. We use $\mathcal{F}(\theta,\phi)$ to define the normalized effective steradians Ω_i that can contribute to calculating each velocity component:

$$\Omega_i = \frac{1}{2\pi}\int_0^{2\pi}\int_0^{\pi} \mathcal{F}(\theta,\phi)\ |J_i(\theta,\phi)|\sin\theta\ \mathrm{d}\theta\mathrm{d}\phi$$

where i is a direction (e.g., $\mathrm{X_{MSM'}}$) and $J_i(\theta,\phi)$ is the expression of unit vector $\hat{i}$ in spherical coordinates (e.g., $J_x(\theta,\phi)=\sin\theta\cos\phi$). The parameter Ω_i has the range [0,1] and communicates the weight of the missing regions in determining the velocity component V_i. If $\Omega_i \sim 1$ then any unobserved directions in the composite distribution have little or no effect in determining V_i. Conversely, $\Omega_i \sim 0$ indicates that there is little or no information available to determine V_i. It is worth noting that Ω_i of different velocity components are not independent; $\Omega_x \equiv 1$ requires both $\Omega_y = 1$ and $\Omega_z = 1$. For the distribution in Figure B1a, $\Omega_x = 0.84$, $\Omega_y = 0.96$, and $\Omega_z = 0.98$, that is, the distribution is practically complete along $Y_{\mathrm{MSM'}}$ and $Z_{\mathrm{MSM'}}$ with the missing regions mostly affecting $X_{\mathrm{MSM'}}$. Figure B1b is less complete in coverage and has $\Omega_x = 0.44$, $\Omega_y = 0.60$, and $\Omega_z = 0.59$. Finally, we define the symmetry ratio Φ_i:

$$\Phi_i = \frac{1-|\omega_i|}{1+|\omega_i|}$$

where

$$\omega_i = \frac{1}{2\pi\Omega_i}\int_0^{2\pi}\int_0^{\pi} \mathcal{F}(\theta,\phi)\ J_i(\theta,\phi)\sin\theta\ \mathrm{d}\theta\mathrm{d}\phi$$

is the normalized difference in effective steradians between the $\pm i$ directions. The parameter Φ_i has the range $[(2\Omega_i - 1) > 0,1]$ and communicates the relative symmetry of Ω_i between the $\pm i$ directions. In other words, $\Phi_i = 1$ indicates that there is no asymmetry in the observed portions of the distribution between $+i$ and $-i$, while $\Phi_i = 0$ indicates that all observed portions of the distribution are in one hemisphere (e.g., only observations of $+i$ and none of $-i$). A $\Phi_i = 0.5$ value indicates that one hemisphere (e.g., $+i$) has twice the observed velocity space contributing to determining V_i than the other hemisphere ($-i$). Figure B1a has $\Phi_x = 0.91$, $\Phi_y = 0.98$, and $\Phi_z = 1.00$, while Figure B1b has $\Phi_x = 0.85$, $\Phi_y = 0.41$, and $\Phi_z = 0.25$. In other words, while there is little or no bias along any direction in Figure B1a, there is substantial asymmetry along $\pm Y_{\mathrm{MSM'}}$ and $\pm Z_{\mathrm{MSM'}}$ in Figure B1b. Used together, Ω_i and Φ_i indicate how *complete* and *unbiased*, respectively, the velocity space distribution is for determining V_i.

We use the FIPS software model to set thresholds on Ω_i and Φ_i for calculating and displaying velocity components (e.g., Figure 3). With a set of input plasma moments, we use the software model to generate a complete velocity space distribution to which we apply missing angular regions and calculate resulting plasma moments. We generate 12.4 million unique combinations of plasma moments and velocity space coverage to determine how the coverage affects determination of plasma moments. To keep root-mean-squared errors in V_i less than either 25% or 25 km/s (whichever is greater for a given set of plasma moments) requires $\Omega_i > 0.4$ and $\Phi_i > 0.7$. Above these thresholds, errors in proton density are less than 8% or 0.1 $\mathrm{cm^{-3}}$ and errors in proton temperature are less than 20% or 2 MK. We implement these thresholds in calculating and displaying statistical plasma flows in Figure 3. If either Ω_i or Φ_i for a given flow component is below its threshold, we do not display that flow component in Figure 3 (i.e., it is displayed as a gray bin). If both Ω_i and Φ_i are above their thresholds, then we display the flow component and incorporate the uncertainty from the missing velocity space regions with the statistical and systematic uncertainties already prescribed by Dewey et al. (2018). For the example distributions in Figure B1, we calculate and display all three flow components from the distribution in Figure B1a, but only calculate and display the V_x component in Figure B1b.

Data Availability Statement

All MESSENGER data used in this study are available from the NASA Planetary Data System at this site (https://pds-ppi.igpp.ucla.edu/search/?sc=Messenger).

Acknowledgments
NASA's Earth and Space Science Fellowship Program (80NSSC17K0493) supported R. M. Dewey. NASA Grants NNX16AJ67G and 80NSSC18K1137 supported W. Sun and J. A. Slavin. NASA Discovery Data Analysis Grant NNX16AJ05G supported J. M. Raines. A. R. Azari was supported by the National Science Foundation Graduate Research Fellowship Program under Grant DGE 1256260. R. M. Dewey would like to thank A. Runov, A. Artemyev, C. Gabrielse, V. Angelopoulos, and T. Nishimura for valuable conversations.

References

Anderson, B. J., Acuña, M. H., Lohr, D. A., Scheifele, J., Raval, A., Korth, H., & Slavin, J. A. (2007). The magnetometer instrument on MESSENGER. *Space Science Reviews*, *131*(1–4), 417–450. https://doi.org/10.1007/s11214-007-9246-7

Anderson, B. J., Johnson, C. L., Korth, H., Purucker, M. E., Winslow, R. M., Slavin, J. A., et al. (2011). The global magnetic field of mercury from MESSENGER orbital observations. *Science*, *333*(6051), 1859–1862. https://doi.org/10.1126/science.1211001

Anderson, B. J., Johnson, C. L., Korth, H., Slavin, J. A., Winslow, R. M., Phillips, R. J., et al. (2014). Steady-state field-aligned currents at mercury. *Geophysical Research Letters*, *41*, 7444–7452. https://doi.org/10.1002/2014GL061677

Andrews, G. B., Zurbuchen, T. H., Mauk, B. H., Malcom, H., Fisk, L. A., Gloeckler, G., et al. (2007). The energetic particle and plasma spectrometer instrument on the MESSENGER spacecraft. *Space Science Reviews*, *131*(1–4), 523–556. https://doi.org/10.1007/s11214-007-9272-5

Angelopoulos, V., Baumjohann, W., Kennel, C. F., Coroniti, F. V., Kivelson, M. G., Pellat, R., et al. (1992). Bursty bulk flows in the inner central plasma sheet. *Journal of Geophysical Research*, *97*(A4), 4027–4039. https://doi.org/10.1029/91JA02701

Ashour-Abdalla, M., El-Alaoui, M., Goldstein, M. L., Zhou, M., Schriver, D., Richard, R., et al. (2011). Observations and simulations of non-local acceleration of electrons in magnetotail magnetic reconnection events. *Nature Physics*, *7*(4), 360–365. https://doi.org/10.1038/nphys1903

Azari, A. R., Liemohn, M. W., Jia, X., Thomsen, M. F., Mitchell, D. G., Sergis, N., et al. (2018). Interchange injections at Saturn: Statistical survey of energetic H+ sudden flux intensifications. *Journal of Geophysical Research: Space Physics*, *123*, 4692–4711. https://doi.org/10.1029/2018JA025391

Baumjohann, W., Hesse, M., Kokubun, S., Mukai, T., Nagai, T., & Petrukovich, A. A. (1999). Substorm dipolarization and recovery. *Journal of Geophysical Research*, *104*(A11), 24,995–25,000. https://doi.org/10.1029/1999JA900282

Birn, J., Hesse, M., Haerendel, G., Aumjohann, W. B., & Shiokawa, K. (1999). Flow braking and the substorm current wedge. *Journal of Geophysical Research*, *114*(A), 19,895–19,904.

Birn, J., Hesse, M., Nakamura, R., & Zaharia, S. (2013). Particle acceleration in dipolarization events. *Journal of Geophysical Research: Space Physics*, *118*, 1960–1971. https://doi.org/10.1002/jgra.50132

Birn, J., Liu, J., Runov, A., Kepko, L., & Angelopoulos, V. (2019). On the contribution of dipolarizing flux bundles to the substorm current wedge and to flux and energy transport. *Journal of Geophysical Research: Space Physics*, *124*, 5408–5420. https://doi.org/10.1029/2019JA026658

Birn, J., Nakamura, R., Panov, E., & Hesse, M. (2011). Bursty bulk flows and dipolarization in MHD simulations of magnetotail reconnection. *Journal of Geophysical Research*, *116*, A01210. https://doi.org/10.1029/2010JA016083

Delcourt, D. (2013). On the supply of heavy planetary material to the magnetotail of mercury. *Annales Geophysicae*, *31*(10), 1673–1679. https://doi.org/10.5194/angeo-31-1673-2013

Delcourt, D. C., Grimald, S., Leblanc, F., Berthelier, J.-J., Millilo, A., Mura, A., et al. (2003). A quantitative model of planetary Na+ contribution to Mercury's magnetosphere. *Annales Geophysicae*, *21*(8), 1723–1736. https://doi.org/10.5194/angeo-21-1723-2003

Dewey, R. M., Raines, J. M., Sun, W., Slavin, J. A., & Poh, G. (2018). MESSENGER observations of fast plasma flows in Mercury's magnetotail. *Geophysical Research Letters*, *45*, 10,110–10,118. https://doi.org/10.1029/2018GL079056

Dewey, R. M., Raines, J. M., & Tracy, P. J. (2017). Interpreting FIPS density, temperature, and pressure. NASA planetary data system, MESS-E/V/H/SW-EPPS-3-FIPS-DDR-V2.0.

Dewey, R. M., Slavin, J. A., Raines, J. M., Baker, D. N., & Lawrence, D. J. (2017). Energetic electron acceleration and injection during dipolarization events in Mercury's magnetotail. *Journal of Geophysical Research: Space Physics*, *122*, 12,170–12,188. https://doi.org/10.1002/2017JA024617

DiBraccio, G. A., Slavin, J. A., Boardsen, S. A., Anderson, B. J., Korth, H., Zurbuchen, T. H., et al. (2013). MESSENGER observations of magnetopause structure and dynamics at Mercury. *Journal of Geophysical Research: Space Physics*, *118*, 997–1008. https://doi.org/10.1002/jgra.50123

DiBraccio, G. A., Slavin, J. A., Imber, S. M., Gershman, D. J., Raines, J. M., Jackman, C. M., et al. (2015). MESSENGER observations of flux ropes in Mercury's magnetotail. *Planetary and Space Science*, *115*, 77–89. https://doi.org/10.1016/j.pss.2014.12.016

Dubyagin, S., Sergeev, V., Apatenkov, S., Angelopoulos, V., Runov, A., Nakamura, R., et al. (2011). Can flow bursts penetrate into the inner magnetosphere? *Geophysical Research Letters*, *38*, L08102. https://doi.org/10.1029/2011GL047016

Fu, H. S., Cao, J. B., Khotyaintsev, Y. V., Sitnov, M. I., Runov, A., Fu, S. Y., et al. (2013). Dipolarization fronts as a consequence of transient reconnection: In situ evidence. *Geophysical Research Letters*, *40*, 6023–6027. https://doi.org/10.1002/2013GL058620

Gabrielse, C., Harris, C., Angelopoulos, V., Artemyev, A., & Runov, A. (2016). The role of localized inductive electric fields in electron injections around dipolarizing flux bundles. *Journal of Geophysical Research: Space Physics*, *121*, 9560–9585. https://doi.org/10.1002/2016JA023061

Gershman, D. J., Slavin, J. A., Raines, J. M., Zurbuchen, T. H., Anderson, B. J., Korth, H., et al. (2013). Magnetic flux pileup and plasma depletion in Mercury's subsolar magnetosheath. *Journal of Geophysical Research: Space Physics*, *118*, 7181–7199. https://doi.org/10.1002/2013JA019244

Imber, S. M., & Slavin, J. A. (2017). MESSENGER observations of magnetotail loading and unloading: Implications for substorms at Mercury. *Journal of Geophysical Research: Space Physics*, *122*, 11,402–11,412. https://doi.org/10.1002/2017JA024332

Janhunen, P., & Kallio, E. (2004). Surface conductivity of mercury provides current closure and may affect magnetospheric symmetry. *Annals of Geophysics*, *22*(5), 1829–1837. https://doi.org/10.5194/angeo-22-1829-2004

Jia, X., Slavin, J. A., Gombosi, T. I., Daldorff, L. K. S., Toth, G., & van der Holst, B. (2015). Global MHD simulations of Mercury's magnetosphere with coupled planetary interior: Induction effect of the planetary conducting core on the global interaction. *Journal of Geophysical Research: Space Physics*, *120*, 4763–4775. https://doi.org/10.1002/2015JA021143

Jia, X., Slavin, J. A., Poh, G., DiBraccio, G. A., Toth, G., Chen, Y., et al. (2019). MESSENGER observations and global simulations of highly compressed magnetosphere events at Mercury. *Journal of Geophysical Research: Space Physics*, *124*, 229–247. https://doi.org/10.1029/2018JA026166

Johnson, C. L., Philpott, L. C., Anderson, B. J., Korth, H., Hauck, S. A. II, Heyner, D., et al. (2016). Messenger observations of induced magnetic fields in Mercury's core. *Geophysical Research Letters*, *43*, 2436–2444. https://doi.org/10.1002/2015GL067370

Karlsson, T., Hamrin, M., Nilsson, H., Kullen, A., & Pitkänen, T. (2015). Magnetic forces associated with bursty bulk flows in Earth's magnetotail. *Geophysical Research Letters*, *42*, 3122–3128. https://doi.org/10.1002/2015GL063999

Kaymaz, Z., Siscoe, G. L., & Luhmann, J. G. (1992). IMF draping around the Geotail: IMP 8 observations. *Journal of Geophysical Research*, *19*(8), 829–832. https://doi.org/10.1029/92GL00403

Kepko, L., Glassmeier, K.-H., Slavin, J. A., & Sundberg, T. (2015). Substorm current wedge at Earth and Mercury. In A. Keiling, C. M. Jackman, & P. A. Delamere (Eds.), *Magnetotails in the solar system* (pp. 361–372). Hoboken, NJ: John Wiley. https://doi.org/10.1002/9781118842324.ch21

Kepko, L., McPherron, R., Amm, O., Apatenkov, S., Baumjohann, W., Birn, J., & Sergeev, V. (2015). Substorm current wedge revisited. *Space Science Reviews*, *190*(1-4), 1–46. https://doi.org/10.1007/s11214-014-0124-9

Korth, H., Anderson, B. J., Gershman, D. J., Raines, J. M., Slavin, J. A., Zurbuchen, T. H., et al. (2014). Plasma distribution in Mercury's magnetosphere derived from MESSENGER magnetometer and fast imaging plasma spectrometer observations. *Journal of Geophysical Research: Space Physics*, *119*, 2917–2932. https://doi.org/10.1002/2013JA019567

Korth, H., Anderson, B. J., Johnson, C. L., Slavin, J. A., Raines, J. M., & Zurbuchen, T. H. (2018). Structure and configuration of Mercury's magnetosphere. In S. C. L. R. Nittler, & B. J. Anderson (Eds.), *Mercury: The view after MESSENGER* (Chap 16, pp. 430–460). London: Cambridge Univ. Press. ISBN: 978-1107154452

Liu, J., Angelopoulos, V., Runov, A., & Zhou, X.-Z. (2013). On the current sheets surrounding dipolarizing flux bundles in the magnetotail: The case for wedgelets. *Journal of Geophysical Research: Space Physics*, *118*, 2000–2020. https://doi.org/10.1002/jgra.50092

Liu, J., Angelopoulos, V., Zhou, X.-Z., & Runov, A. (2014). Magnetic flux transport by dipolarizing flux bundles. *Journal of Geophysical Research: Space Physics*, *119*, 909–926. https://doi.org/10.1002/2013JA019395

McPherron, R. L., Russell, C. T., & Aubry, M. A. (1973). Satellite studies of magnetospheric substorms on August 15, 1968, 9, Phenomenological model for substorms. *Journal of Geophysical Research*, *78*, 3131.

Merkin, V. G., Panov, E. V., Sorathia, K., & Ukhorskiy, A. Y. (2019). Contribution of bursty bulk flows to the global dipolarization of the magnetotail during an isolated substorm. *Journal of Geophysical Research: Space Physics*, *124*, 8647–8668. https://doi.org/10.1029/2019JA026872

Nakamura, M. S., Matsumoto, H., & Fujimoto, M. (2002). Interchange instability at the leading part of reconnection jets. *Geophysical Research Letters*, *29*(8), 1247. https://doi.org/10.1029/2001GL013780

Nakamura, R., Baumjohann, W., Mouikis, C., Kistler, L. M., Runov, A., Volwerk, M., & Balogh, A. (2004). Spatial scale of high-speed flows in the plasma sheet observed by Cluster. *Geophysical Research Letters*, *31*, L09804. https://doi.org/10.1029/2004GL019558

Ogilvie, K. W., Scudder, J. D., Vasyliunas, V. M., Hartle, R. E., & Siscoe, G. L. (1977). Observations at the planet mercury by the plasma electron experiment, Mariner 10. *Journal of Geophysical Research*, *82*(13), 1807–1824. https://doi.org/10.1029/JA082i013p01807

Ohtani, S., Singer, H. J., & Mukai, T. (2006). Effects of the fast plasma sheet flow on the geosynchronous magnetic configuration: Geotail and GOES coordinated study. *Journal of Geophysical Research*, *111*, A01204. https://doi.org/10.1029/2005JA011383

Panov, E. V., Baumjohann, W., Nakamura, R., Kubyshkina, M. V., Glassmeier, K.-H., Angelopoulos, V., et al. (2014). Period and damping factor of Pi2 pulsations during oscillatory flow braking in the magnetotail. *Journal of Geophysical Research: Space Physics*, *119*, 4512–4520. https://doi.org/10.1002/2013JA019633

Parks, G. K., Lee, E., Lin, N., Mozer, F., Wilber, M., Dandouras, I., et al. (2007). Solitary electromagnetic pulses detected with super-Alfvénic flows in Earth's geomagnetic tail. *Physical Review Letters*, *98*(26), 98. https://doi.org/10.1103/PhysRevLett.98.265001

Poh, G., Slavin, J. A., Jia, X., Raines, J. M., Imber, S. M., Sun, W.-J., et al. (2017a). Mercury's cross-tail current sheet: Structure, X-line location and stress balance. *Geophysical Research Letters*, *44*, 678–686. https://doi.org/10.1002/2016GL071612

Poh, G., Slavin, J. A., Jia, X., Raines, J. M., Imber, S. M., Sun, W.-J., et al. (2017b). Coupling between Mercury and its nightside magnetosphere: Cross-tail current sheet asymmetry and substorm current wedge formation. *Journal of Geophysical Research: Space Physics*, *122*, 8419–8433. https://doi.org/10.1002/2017JA024266

Poh, G., Slavin, J. A., Jia, X., Sun, W.-J., Raines, J. M., Imber, S. M., et al. (2018). Transport of mass and energy in Mercury's plasma sheet. *Geophysical Research Letters*, *45*, 12,163–12,170. https://doi.org/10.1029/2018GL080601

Pulkkinen, A., Rastätter, L., Kuznetsova, M., Singer, H., Balch, C., Weimer, D., et al. (2013). Community-wide validation of geospace model ground magnetic field perturbation predictions to support model transition to operations. *Space Weather*, *11*, 369–385. https://doi.org/10.1002/swe.20056

Raines, J. M., Gershman, D. J., Slavin, J. A., Zurbuchen, T. H., Korth, H., Anderson, B. J., & Solomon, S. C. (2014). Structure and dynamics of Mercury's magnetospheric cusp: MESSENGER measurements of protons and planetary ions. *Journal of Geophysical Research: Space Physics*, *119*, 6587–6602. https://doi.org/10.1002/2014JA020120

Raines, J. M., Gershman, D. J., Zurbuchen, T. H., Sarantos, M., Slavin, J. A., Gilbert, J. A., et al. (2013). Distribution and compositional variations of plasma ions in Mercury's space environment: The first three Mercury years of MESSENGER observations. *Journal of Geophysical Research: Space Physics*, *118*, 1604–1619. https://doi.org/10.1029/2012JA018073

Raines, J. M., Slavin, J. A., Tracy, P., Gershman, D. J., Zurbuchen, T., Dewey, R. M., & Sarantos, M. (2016). Plasma precipitation on Mercury's nightside and its implications for magnetospheric convection and exosphere generation. *AGU Fall Meeting 2016*. Paper #SM53B-08, San Francisco, CA

Raines, J. M., Slavin, J. A., Zurbuchen, T. H., Gloeckler, G., Anderson, B. J., Baker, D. N., et al. (2011). MESSENGER observations of the plasma environment near mercury. *Planetary and Space Science*, *59*(15), 2004–2015. https://doi.org/10.1016/j.pss.2011.02.004

Rong, Z. J., Ding, Y., Slavin, J. A., Zhong, J., Poh, G., Sun, W. J., et al. (2018). The magnetic field structure of Mercury's magnetotail. *Journal of Geophysical Research: Space Physics*, *123*, 548–566. https://doi.org/10.1002/2017JA024923

Runov, A., Angelopoulos, V., Gabrielse, C., Liu, J., Turner, D. L., & Zhou, X.-Z. (2015). Average thermodynamic and spectral properties of plasma in and around dipolarizing flux bundles. *Journal of Geophysical Research: Space Physics*, *120*, 4369–4383. https://doi.org/10.1002/2015JA021166

Runov, A., Angelopoulos, V., Gabrielse, C., Zhou, X.-Z., Turner, D., & Plaschkle, F. (2013). Electron fluxes and pitch-angle distributions at dipolarization fronts: THEMIS multipoint observations. *Journal of Geophysical Research: Space Physics*, *118*, 744–755. https://doi.org/10.1002/jgra.50121

Runov, A., Angelopoulos, V., Sitnov, M. I., Sergeev, V. A., Bonnell, J., McFadden, J. P., et al. (2009). THEMIS observations of an earthward-propagating dipolarization front. *Geophysical Research Letters*, *36*, L14106. https://doi.org/10.1029/2009GL038980

Runov, A., Angelopoulos, V., & Zhou, X.-Z. (2012). Multipoint observations of dipolarization front formation by magnetotail reconnection. *Journal of Geophysical Research*, *117*, A05230. https://doi.org/10.1029/2011JA017361

Sergeev, V. A., Angelopoulos, V., Gosling, J. T., Cattell, C. A., & Russell, C. T. (1996). Detection of localized, plasma-depleted flux tubes or bubbles in the midtail plasma sheet. *Journal of Geophysical Research*, *101*(A5), 10,817–10,826. https://doi.org/10.1029/96JA00460

Shiokawa, K., Baumjohann, W., & Haerendel, G. (1997). Braking of high-speed flows in the near-earth tail. *Geophysical Research Letters*, *24*(10), 1179–1182. https://doi.org/10.1029/97GL01062

Shue, J.-H., Song, P., Russell, C. T., Steinberg, J. T., Chao, J. K., Zastenker, G., et al. (1998). Magnetopause location under extreme solar wind conditions. *Journal of Geophysical Research*, *103*(A8), 17,691–17,700. https://doi.org/10.1029/98JA01103

Sitnov, M. I., Swisdak, M., & Divin, A. V. (2009). Dipolarization fronts as a signature of transient reconnection in the magnetotail. *Journal of Geophysical Research*, *114*, A04202. https://doi.org/10.1029/2008JA013980

Slavin, J. A., Acuna, M. H., Anderson, B. J., Baker, D. N., Benna, M., Boardsen, S. A., et al. (2009). MESSENGER observations of magnetic reconnection in Mercury's magnetosphere. *Science*, *324*(5927), 606–610. https://doi.org/10.1126/science.1172011

Slavin, J. A., Anderson, B. J., Baker, D. N., Benna, M., Boardsen, S. A., Gloeckler, G., et al. (2010). MESSENGER observations of extreme loading and unloading of Mercury's magnetic tail. *Science*, *329*(5992), 665–668. https://doi.org/10.1126/science.1188067

Slavin, J. A., Anderson, B. J., Baker, D. N., Benna, M., Boardsen, S. A., Gold, R. E., et al. (2012). MESSENGER and mariner 10 flyby observations of magnetotail structure and dynamics at mercury. *Journal of Geophysical Research*, *117*, A01215. https://doi.org/10.1029/2011JA016900

Slavin, J. A., Baker, D. N., Gershman, D. J., Ho, G., Imber, S. M., Krimigis, S. M., & Sundberg, T. (2018). Mercury's dynamic magnetosphere. In S. C. L. R. Nittler, & B. J. Anderson (Eds.), *Mercury: The view after MESSENGER* (Chap 17, pp. 461–496). London: Cambridge Univ. Press. ISBN: 978-1107154452

Slavin, J. A., DiBraccio, G. A., Gershman, D. J., Imber, S., Poh, G. K., Raines, J., et al. (2014). MESSENGER observations of Mercury's dayside magnetosphere under extreme solar wind conditions. *Journal of Geophysical Research: Space Physics*, *119*, 8087–8116. https://doi.org/10.1002/2014JA020319

Slavin, J. A., & Holzer, R. E. (1981). Solar wind flow about the terrestrial planets, 1. Modeling bow shock position and shape. *Journal of Geophysical Research*, *86*(A13), 11401–11,418. https://doi.org/10.1029/JA086iA13p11401

Smith, A. W., Slavin, J. A., Jackman, C. M., Poh, G.-K., & Fear, R. C. (2017). Flux ropes in the Hermean magnetotail: Distribution, properties, and formation. *Journal of Geophysical Research: Space Physics*, *122*, 8136–8153. https://doi.org/10.1002/2017JA024295

Southwood, D. J., & Kivelson, M. G. (1991). An approximate description of field-aligned currents in a planetary magnetic field. *Journal of Geophysical Research*, *96*(A1), 67–75. https://doi.org/10.1029/90ja01806

Sun, W. J., Fu, S. Y., Parks, G. K., Liu, J., Yao, Z. H., Shi, Q. Q., et al. (2013). Field-aligned currents associated with dipolarizations fronts. *Geophysical Research Letters*, *40*, 4503–4508. https://doi.org/10.1002/grl.50902

Sun, W. J., Fu, S. Y., Slavin, J. A., Raines, J. M., Zong, Q. G., Poh, G. K., & Zurbuchen, T. H. (2016). Spatial distribution of Mercury's flux ropes and reconnection fronts: MESSENGER observations. *Journal of Geophysical Research: Space Physics*, *121*, 7590–7607. https://doi.org/10.1002/2016JA022787

Sun, W. J., Raines, J. M., Fu, S. Y., Slavin, J. A., Wei, Y., Poh, G. K., et al. (2017). MESSENGER observations of the energization and heating of protons in the near-Mercury magnetotail. *Geophysical Research Letters*, *44*, 8149–8158. https://doi.org/10.1002/2017GL074276

Sun, W. J., Slavin, J. A., Dewey, R. M., Chen, Y., DiBraccio, G. A., Raines, J. M., et al. (2020). MESSENGER Observations of Mercury's Nightside Magnetosphere under Extreme Solar Wind Conditions: Reconnection-Generated Structures and Steady Convection. *Journal of Geophysical Research: Space Physics*, *125*, e2019JA027490. https://doi.org/10.1029/2019JA027490

Sun, W. J., Slavin, J. A., Dewey, R. M., Raines, J. M., Fu, S. Y., Wei, Y., et al. (2018). A comparative study of the proton properties of magnetospheric substorms at earth and mercury in the near magnetotail. *Geophysical Research Letters*, *45*, 7933–7941. https://doi.org/10.1029/2018GL079181

Sun, W.-J., Slavin, J. A., Fu, S., Raines, J. M., Sundberg, T., Zong, Q. G., et al. (2015). MESSENGER observations of Alfvénic and compressional waves during Mercury's substorms. *Geophysical Research Letters*, *42*, 6189–6198. https://doi.org/10.1002/2015GL065452

Sundberg, T., Slavin, J. A., Boardsen, S. A., Anderson, B. J., Korth, H., Ho, G. C., et al. (2012). MESSENGER observations of dipolarization events in Mercury's magnetotail. *Journal of Geophysical Research*, *117*, A00M03. https://doi.org/10.1029/2012JA017756

Ukhorskiy, A. Y., Sorathia, K. A., Merkin, V. G., Sitnov, M. I., Mitchell, D. G., & Gkioulidou, M. (2018). Ion trapping and acceleration at dipolarization fronts: High-resolution MHD and test-particle simulations. *Journal of Geophysical Research: Space Physics*, *123*, 5580–5589. https://doi.org/10.1029/2018JA025370

Winslow, R. M., Anderson, B. J., Johnson, C. L., Slavin, J. A., Korth, H., Purucker, M. E., et al. (2013). Mercury's magnetopause and bow shock from MESSENGER magnetometer observations. *Journal of Geophysical Research: Space Physics*, *118*, 2213–2227. https://doi.org/10.1002/jgra.50237

Zhong, J., Wan, W. X., Wei, Y., Slavin, J. A., Raines, J. M., Rong, Z. J., et al. (2015). Compressibility of Mercury's dayside magnetosphere. *Geophysical Research Letters*, *42*, 10,135–10,139. https://doi.org/10.1002/2015GL067063